Tsunami Induced by the Strike-Slip Fault of the 2018 Palu Earthquake (Mw=7.5), Sulawesi Island, Indonesia

Tung-Cheng Ho[1]*, Kenji Satake[1], Shingo Watada[1], Ming-Che Hsieh[2], Ray Y. Chuang[3], Yosuke Aoki[1], Iyan E. Mulia[1], Aditya Riadi Gusman[4], Chih-Heng Lu[3]

[1]Earthquake Research Institute, the University of Tokyo, Tokyo, Japan.

[2]Disaster Prevention Technology Research Center, Sinotech Engineering Consultants, Taipei, Taiwan.

[3]Department of Geography, National Taiwan University, Taipei, Taiwan.

[4]GNS Science, Lower Hutt, New Zealand.

Corresponding author: Tung-Cheng Ho (dong@eri.u-tokyo.ac.jp)

*Now at Disaster Prevention Research Institute (DPRI), Kyoto University.

Key Points:

- The two-step analysis of teleseismic, SAR, and tsunami data retrieves an earthquake source model that explains the observed tsunami.
- A strike-slip fault with localized large dip slip of the 2018 Palu earthquake induced the devastating regional tsunami.
- Onshore strike-slip faults should also be regarded as a potential source of tsunami for regional areas.

Abstract

An unusual devastating tsunami occurred on 28 September 2018 after a strike-slip faulting earthquake in Sulawesi, Indonesia. The induced tsunami struck Palu city with 4-m wave height and flow depth. We performed a two-step analysis to investigate the source of the tsunami. We first conducted the teleseismic source inversion and obtained the slip distribution of the strike-slip fault. Our tsunami simulation from the coseismic deformation of the seismically-estimated strike-slip faulting produced a tsunami comparable to the leading part of the observation at Pantoloan. We then jointly utilized the tsunami waveform and Synthetic Aperture Radar (SAR) data to reconstruct the detailed slip distribution on the fault plane. Because of the lack of SAR data in the bay, the tsunami data is necessary to constrain the offshore slip distribution, which directly induces the tsunami. The inverted source model shows a strike-slip fault which consists of three segments extending from the epicenter to the south of 1.4°S with two bends and two asperities around Palu city. The joint inversion model accurately reconstructs the observed surface displacements and the leading part of the

tsunami waveform. Our result exhibits the significant contribution of the strike-slip faulting to the tsunami, but it also suggests additional tsunami sources, such as landslides, for the high inundations near Palu bay. The result also indicates that regional devastating tsunamis can result from an onshore strike-slip fault with localized large dip slip.

Plain Language Summary

The Palu, Indonesia, earthquake of 28 September 2018 produced tsunami flooding and damage in Palu city. Because of its strike-slip mechanism, which is not efficient to produce tsunamis, multiple submarine landslides have been speculated as a tsunami source. We found that the fault model estimated by teleseismic waves (recorded globally outside Indonesia) can reproduce the tsunami recorded at the Pantoloan station in Palu bay. This indicates that the source of tsunami recoded at Pantoloan is mostly the fault motion accompanied by the earthquake. We then combined the displacements measured by Synthetic Aperture Radar images and the Pantoloan tsunami waveform to estimate the slip distribution on the fault. The slip model shows a strike-slip fault with two large slip areas located near Palu city between two bends. This model well reproduces the Pantoloan tsunami but fails to fully reproduce the inundations in Palu city, suggesting that additional tsunami sources, such as landslides, should be responsible for the large inundations in Palu city. Our result suggests that a strike-slip fault can induce a devastating local tsunami.

1 Introduction

On September 28, 2018, a devastating tsunami impacted Palu city, Sulawesi Island, Indonesia (Figure 1) after an M7.5 earthquake. A moment tensor solution obtained by the U.S. Geological Survey (USGS) from W phase waveforms suggests strike-slip faulting with a high dip angle (~67°) at al shallow depth (~13km). The estimated nodal plane strikes approximately north-south (N10°W) with a rake angle of -17°, implying the presence of some normal faulting component.

The Palu-Koro fault (Figure 1), the plate boundary between the Makassar block and the North Sula block, is thought to be responsible for the Palu earthquake. Global Navigation Satellite System (GNSS) monitoring shows that the relative velocity on the Palu-Koro fault zone accommodates 42 mm/yr of a complex transtensive motion with a 39 mm/yr of strike-slip and 11-14 mm/yr of extension (Socquet et al., 2006). Three tsunami events associated with the Palu-Koro fault zone have been reported in 1927, 1968, and 1996, of which the 1927 and 1968 earthquakes also caused destructive tsunamis in Palu bay (Prasetya et al., 2001). Socquet et al. (2019) and Bao et al. (2019) pointed out that the 2018 earthquake might have ruptured with a supershear velocity from the back-projection of the seismic wavefield and the geodetic data.

A slip distribution obtained by USGS from teleseismic waveforms (United States Geological Survey, 2018) suggests an asperity with a maximum of more than 8 m slip under Palu bay. The source time function shows that most of the moment was released within 30 s after the earthquake origin time. Socquet et al. (2019) utilized horizontal offsets in SAR images to estimate the slip distribution and indicated a peak slip of more than 5 m of strike-slip and 2 m of reverse faulting dip-slip near the asperity.

Devastating tsunami inundations impacted the areas around Palu bay after the earthquake. High runups were measured by field surveys (Muhari et al., 2018; Omira et al., 2019; Yalciner et al., 2018; Paulik et al., 2019; Mikami et al., 2019). Flow depths of up to 5 m on the south coast of Palu bay (Palu City), up to 2 m observed on the east coast, and higher than 1 m on the west coast were observed. The tsunami waveform was recorded in the bay by

a tide gauge at the port of Pantoloan (Figure 1). The other tide gauge located ~200 km outside of the bay at Mamuju recorded tsunami waves from about 20 minutes after the earthquake origin time. However, numerical simulations showed that the tsunami waves take at least 40 minutes from the source area to the Mamuju station (Heidarzadeh et al., 2019). Therefore, the tsunami recorded at the Mamuju station is not considered to be directly originated from the earthquake.

Sassa and Takagawa (2019) indicated that the earthquake caused extensive liquefaction which induced liquefied sediment flows in the coastal area, resulting in the devastating tsunami. Heidarzadeh et al. (2019) performed tsunami simulation using the source model of USGS (United States Geological Survey, 2018). They fairly well reconstructed the tsunami waveform at Pantoloan although the wave height was slightly underestimated. They mentioned that a large submarine landslide may intensify the tsunami. Gusman et al. (2019) focused on the vertical displacements around the narrow bay that generated the tsunami. They concluded that the tsunami inundation was caused by a combination of the earthquake faulting, landslides, and the high tide time of the event.

Ulrich et al. (2019) used a physics-based, coupled earthquake-tsunami model to demonstrate that the tsunami wave and inundations were mainly generated by the earthquake deformation and suggested that landslide may not be the primary source of the tsunami. Fang et al. (2019) investigated the source geometry and rupture using the SAR interferometry (InSAR) of ALOS-2 images and regional broadband seismograms. Their rupture model shows a rupture propagated mainly southward and a major asperity located at the south of Palu bay with a maximum slip of 6.5 m. They concluded that the offshore asperities with significant normal-slip components are responsible for the tsunami.

Yolsal-Çevikbilen et al. (2019) inverted the teleseismic waveforms to estimate the slip distribution. Their model shows an asperity concentrated in the bay area, and they suggested that the normal faulting could be partially responsible for the tsunami in Palu bay. However, Lee et al. (2019) expected a smaller tsunami than the observation from their inversion of teleseismic waveforms. Besides coseismic effects, they suggested that other sources, such as a submarine landslide, are possible to account for the local tsunami.

The primary tsunami source is still controversial and the contribution of the earthquake fault motion to the generation of tsunami is not well clarified, although strike-slip faulting is generally considered not to generate a devastating tsunami. To better understand the tsunami generation by a strike-slip fault, we performed a two-step analysis that utilized teleseismic, SAR, and tsunami data to examine the contribution of the fault slip to the tsunami generation and estimate the slip distribution on the fault plane.

2 Data

2.1 Teleseismic Body and Surface Waveforms

The teleseismic records from the Global Seismograph Network (GSN) which provides good azimuthal coverage for inversion (Figure S1) were utilized to estimate the slip distribution of the Palu earthquake. The passbands for the body and surface waves are 1-180 s and 200-500 s, respectively.

2.2 Surface Displacements from SAR Data

Sub-pixel correlation of SAR intensity images before and after an earthquake provide a high-resolution measurement of coseismic surface displacements (e.g., Michel et al., 1999). The azimuth offsets, displacements in the azimuth direction, extracted from the Sentinel-1 satellite images exhibit clear displacement offsets, from which we can constrain the geometry of the surface faulting.

In order to measure coseismic displacements, we used Sentinel-1 satellite images on 7 June 2018 and 5 October 2018 from the descending orbits, and on 13 March 2017 and 4 October 2018 from the ascending orbits. It is difficult to generate interferograms with C-band images due to temporal decorrelation and large surface deformation. Therefore, we used the two Single Look Complex (SLC) radar images, of which pixel spacing is 2.3 m and 14.1 m in the range direction and azimuth direction, respectively, and we calculated the azimuth offset from the correlation between two radar amplitude images by the pixel-tracking method (e.g., Michel et al., 1999). The window size to measure correlations is 128 x 128 pixels and the sampling spacing is 12 x 12 pixels in size to achieve a spatial resolution of 28 m in the range direction (12 x 2.3 m) and 170 m in the azimuth direction (12 x 14.1 m).

The SAR images well exhibited the trace of the rupture on the surface. Figure 2a shows the azimuth offset from the descending images with a maximum of ~8 m relative displacement across the fault, and the ascending image in Figure 2b exhibits the relative displacement of ~5 m. The fault geometry was constrained by the trace on the surface as shown in Figure 2. The strike varies along the fault trace and the rupture can be divided into three segments by a restraining bend near 0.7°S and a releasing bend near 1.2°S. Large offsets appeared between two bends.

Although the displacements obtained from the azimuth offsets contain more noise than interferograms, this method allows us to measure large displacements where InSAR does not work; InSAR cannot provide displacements in places where the displacement coherence is low (Wright et al., 2005). In addition, the average uncertainty of pixel offset is 1/10 of the pixel size in the azimuth and range directions (Michel et al., 1999).

2.3 Tsunami Waveform

We used the tsunami record of the tide gauge at the port of Pantoloan (the location is shown in Figure 1b) maintained by the Geospatial Information Agency (Badan Informasi Geospasial, BIG) of Indonesia. The sea level is recorded every 60 s. We de-tided the raw data by removing the long period (> 3 hr) tidal constituents, but no resampling or interpolation was applied to the observed data. The Pantoloan station observed an arrival of tsunami wave about 4 min after the earthquake with a maximum wave height (trough to crest) up to 4 m (Figure 3).

An obvious waveform change appears about 8 min (after the red-shaded window in Figure 3b) after the earthquake which may result from the combination of waveforms from different sources. Thus, to ensure that only the leading tsunami wave is used, we utilized the record of the first 8 min from the origin time. Although there is only one available station with observed data, the tsunami signal provides important information on the slip offshore area where no SAR observations were available.

3 Method

3.1 Teleseismic Source Inversion

The location of the rupture initiation was fixed at the hypocenter determined by USGS (119.846°E, 0.256°S, 20 km). A simple fault geometry of an east-dipping plane with a strike of 354° and a dip of 66° (see Aki & Richards, 2002 for angle definitions) was adopted for the teleseismic source inversion. The modeled fault plane is rectangular with a length (along the strike) of 205 km and a width (along the down-dip) of 37 km. The fault plane was divided into subfaults with a size of 5 km x 3.7 km. Variable rupture velocities between 1.5 and 4.5 km/s are allowed. To invert for the slip distribution of the Palu earthquake, we computed the Green's functions for the spherically symmetric 1-D velocity model of PREM (Dziewonski & Anderson, 1981) with replacing the shallow layers by the model of CRUST2.0 (Bassin et al., 2000).

The slip distribution was estimated by the wavelet-decomposition inversion technique of Ji et al. (2002). The wavelet-decomposition technique gives an optimal resolution of long- and short-period signals in the time domain, which corresponds to slip zones (i.e. asperities) of different scales on the fault plane. Ji et al. (2002) demonstrated that this method provides relatively robust and well-resolved slip features by resolution analyses. Furthermore, the inversion scheme solves inverse problems with a large number of free parameters based on a grid-search scheme with optimization of the Simulated-Annealing algorithm (Rothman, 1986). Thus, the wavelet-decomposition scheme permits us to invert for the slip amplitude, slip direction, rise-time, and rupture speed simultaneously and efficiently.

3.2 Tsunami Simulation

We computed the tsunami propagation by applying the shallow water equations (SWE), which account for tsunami arrival time and waveforms with high accuracy. Explicit finite-difference methods have been implemented to solve the SWE in numerical models. These SWE models perform fast and efficient computations and have been widely used in tsunami research (Satake et al., 2013; Ho et al., 2019). We applied the validated model JAGURS (Baba et al., 2015) to solve linear SWE for the Green's functions in the inversions and nonlinear SWE for the inundation evaluation.

To evaluate the dispersion effect, we computed the non-dispersive and dispersive tsunami waveform at Pantoloan and compared them with each other. We first assumed a tsunami source comparable to the 2018 Palu earthquake and simulated the tsunami at Pantoloan by applying the linear SWE to obtain a non-dispersive tsunami waveform. We then converted the non-dispersive waveform into a dispersive waveform utilizing the phase-correction method (Watada et al., 2014; Ho et al., 2017). In Figure S2, the dispersive waveform (red dotted line) is almost identical to the non-dispersive waveform (black line). Because the only tide gauge Pantoloan locates in the source area that recorded the tsunami waves a few minutes after the earthquake, we confirmed that the wave dispersion effect is ignorable in this study.

A nested-grid system built in JAGURS was utilized to calculate the waveforms and evaluate the inundation along the shoreline. We utilized three-level nested-layers to acquire accurate calculations where a grid size of 6″ (~180 m) for Layer 1 (Figure 1a), 2″ (~60 m) for Layer 2 (Figure 1b), and 2/3″ (~20 m) for Layer 3 (Figure 1b) were used. The bathymetry for Layer 1 was based on the national bathymetric data of Indonesia (BATNAS) with 6″ spatial resolution. For levels 2 and 3, we used the bathymetric and topographic data with a higher resolution of 0.27″ obtained from the national digital elevation model of Indonesia

(DEMNAS). Both BATNAS and DEMNAS were provided by the BIG of Indonesia. To improve the inundation modeling, the DEM (digital elevation model) of Layer 2 and 3 were further corrected by the high-resolution bathymetric contour and topographic data (see Gusman et al., 2019). We utilized the finest grid, Layer 3, to compute the tsunami Green's functions for our joint inversion.

We introduced a correction term for water depth change due to permanent seafloor deformation to the Green's functions in our inversion. The Pantoloan station located in the source area should be subsided by the permanent vertical seafloor deformation as shown in Gusman et al. (2019). The recorded tsunami waveform contained the sea surface variation (water wave) and the seafloor deformation. To accurately estimate the tsunami source, we applied the correction for coseismic displacement to incorporate the permanent seafloor deformation into the Green's functions.

3.3 Contribution of Horizontal Deformation on Tsunami Generation

We further calculated the vertical water displacement generated by horizontal deformation acting on bathymetric slopes. Although strike-slip faulting generates small vertical displacement, large horizontal deformation can induce additional vertical water displacement in the presence of bathymetric slopes, strengthening tsunamis. The vertical sea surface displacement is given by (Tanioka & Satake, 1996):

$$u_h = u_x \frac{\partial H}{\partial x} + u_y \frac{\partial H}{\partial y},$$

where u_h is the vertical displacement on the sea surface induced by the horizontal deformation of the seafloor, H is the water depth and u_x and u_y are the horizontal seafloor displacements. u_h is positive upward but H is positive downward (depth). The total vertical displacement at the surface of the seawater is represented by $u_{z\prime} = u_h + u_z$, where u_z is the vertical displacement of the seafloor. u_x, u_y, and u_z are calculated by applying the model of Okada (1985). Figure S6 shows the vertical displacement due to horizontal deformation u_h induced by the joint inversion model in section 4.3. Up to 0.6 m of vertical displacements were generated.

3.4 Configuration for Joint Inversion

The fault was divided into three segments by a restraining bend near 0.7°S and a releasing bend near 1.2°S (Figure 2). The strike varies along the fault trace: segment 1 strikes N2°W (358°) extending 50 km southward from the epicenter to the restraining bend near the bay, where the surface displacement shows a rupture extending southwestward to the bay (Figure 2). In segment 2, the strike changed to N8°W (352°) from the offshore area south of the restraining bend and extended another 50 km to the releasing bend at about 1.2°S where large surface displacements are presented. Segment 3 extended 20 km from the releasing bend to approximately 1.4°S with a strike N11°W (349°).

We discretized the fault plane into 4 by 29 subfaults, each of which has a size of 5 km by 5 km with an eastward dip angle of 66°. The rake angle is allowed to vary between -45° and 45° where the strike-slip with normal or reverse components is incorporated. We calculated the Green's functions of azimuth offsets and tsunami waveforms under an assumption of faulting embedded in the elastic half-space theory (Okada, 1985). We then projected the computed surface displacements to the azimuth direction of the SAR satellite and resampled the tsunami Green's functions to match the time interval of observed tsunami waveform.

We applied the nonnegative least-square method with Tikhonov regularization to acquire the slip distribution on the subfaults. In the joint inversion, the equation is given by:

$$\begin{bmatrix} \mathbf{B_S} \\ \mathbf{B_\tau} \\ \mathbf{0} \\ \mathbf{0} \end{bmatrix} = \begin{bmatrix} \mathbf{G_S} \\ \mathbf{G_\tau} \\ \lambda \mathbf{I} \\ \gamma \boldsymbol{L} \end{bmatrix} \boldsymbol{X^T},$$

where $\mathbf{B_S} = \boldsymbol{b}^k$ is the column vector of observed SAR images where $k = 1$ to 2 represents the azimuth offsets of the descending and ascending SAR images, $\mathbf{G_S}$ is the matrix of azimuth offsets Green's functions $\boldsymbol{S}_j^k$, corresponding to the observation $\boldsymbol{b}^k$, from the jth subfault, where $j = 1$ to M, the number of subfaults. $\mathbf{B_\tau} = \beta \boldsymbol{p}$ is the column vector of the observed tsunami waveforms $\boldsymbol{p}$ at Pantoloan weighted by $\beta = 20$. $\mathbf{G_\tau} = \beta \boldsymbol{\eta}_j$ is the matrix of tsunami Green's functions $\boldsymbol{\eta}_j$ for the jth subfault weighted by β. $\boldsymbol{X} = [x_j]$ is the unknown raw vector of the amplitude for the jth subfault, where j counts for columns. The regularization factor $\lambda \mathbf{I} \boldsymbol{X^T}$ stabilizes the inverse problem, where the $\lambda = 1$ and $\mathbf{I}$ is the identity matrix. We adopted Laplacian operator $\gamma \boldsymbol{L} \boldsymbol{X^T} = 0$ as the spatial smooth constraint, where $\gamma = 1$ is used.

4 Results of Two-step Analysis

4.1 Teleseismic Source Inversion

Figure 4 compares observed and synthetic waveforms of 44 body-waves and 41 surface-waves, respectively, indicating that the synthetic waveforms fit well the observed body and surface waves. Figure 5 shows the estimated slip distribution, which presents a single distinct region of slip concentration. This slip distribution suggests that the center of asperity is located at about 50 km south of the hypocenter. The surface projection of asperity is right in the bay, which might account for the induced large tsunami height. The maximum slip in the asperity is about 4.85 m with less slip to the north and below the hypocenter on the fault plane. The spatial slip distribution and its rupture time suggest that a strike-slip rupture propagates obliquely from the hypocenter to the south as a unilateral rupture with an average rupture velocity ~3 km/s. Figure S3 shows the moment rate function of the inversion. The estimated seismic moment is 2.78 x 10^{20} Nm, which is equivalent to M_W 7.56.

The inverted source model was used to compute the tsunami waveform. Figure 6a shows the computed tsunami waveform compared with the observed tsunami at Pantoloan. The coseismic vertical deformation is shown in Figure S5. The computed tsunami waveform is similar to the observed waveform with a slight phase shift and a smaller amplitude. The fact that the observed tsunami waveforms are explained by the computed one from the slip distribution estimated from teleseismic waveforms implies that the observed tsunami was induced directly by the fault slip.

The teleseismic inversion model (Figure 5) reconstructs the teleseismic body and surface waves with a main asperity concentrating near the bay area. However, no asperity was inverted between 1.0°S to 1.4°S where large offsets were observed by SAR. Contrary to slip distribution inverted from SAR images that are well constrained in a shallow depth, the slip distribution obtained from teleseismic waveforms exhibits a general rupture pattern on the whole fault plane. Because we considered wave propagation in the 1-D velocity model and used long-period waves (e.g., 1-180 s for body wave and 200-500 s for surface wave) in our inversion which correspond to wavelengths of hundreds of kilometers, the inversion result reflects an overall response of the fault plane. Thus, the south asperity might not be revealed by the teleseismic inversion.

4.2 SAR-only Inversion

We then estimated the fault slip distribution with only SAR data, which consists of two horizontal-direction displacement fields (N20°W and S20°W). The estimated slip distribution in Figure 7a shows the inverted slip distribution, which was decomposed into dip-slip and strike-slip components presented in Figure 8. The inverted source model exhibits a peak slip of up to 9 m at 1.1°S north of the releasing bend and an asperity with about 7 m slip in Palu bay south of the restraining bend. A smaller asperity with about 5 m slip is located south of the epicenter. Large strike-slip was retrieved at a shallow depth of ~10 km. The dip-slip component is generally small. The maximum dip-slip is located at the south of the epicenter with ~3 m normal slip. Very weak oblique slip was found near the releasing bend, where shows a normal slip up 1.6 m. Weak oblique slip with reverse-slip of about -1.7 m was retrieved in the restraining bend area. Large normal slip was retrieved at ~1.0°S to explain the surface offsets by SAR images (Figure 2).

Figure 6b shows the computed tsunami waveform from the inverted slip model compared with the observation at Pantoloan. The coseismic vertical deformation is shown in Figure S5. The computed tsunami waveform underestimates the observation and fails to match the phase of the first wave. We calculated the characteristic focal mechanism of the fault plane by averaging the moment tensor of all subfaults. The nodal plane strike/dip/rake was 352°/65°/-9°.

4.3 Joint Inversion

To circumvent the poor capability of reconstructing offshore fault slip by SAR images, we performed the joint inversion utilizing the tsunami and SAR data. Because SAR images only provide coseismic surface displacements on land, the derived offshore slip distribution is less constrained than that on land. Tsunami generation is mainly controlled by offshore fault slip; therefore, tsunami data provides good constraint and more information on offshore slip.

The joint inversion (Figure 7b) exhibits a slip distribution similar to the one obtained by the SAR-only inversion (Figure 7a), but the slip is noticeably different in the bay area between 0.65°S and 0.9°S. We decomposed the slip into dip-slip and strike-slip components shown in Figure 9. Compared to the weak oblique slip in the restraining bend estimated by the SAR-only inversion, the joint inversion retrieved strike-slip faulting in the bend area. Very weak oblique slip was again retrieved in the releasing bend area at 1.2°S as retrieved by SAR-only inversion. Large dip-slip normal components of 2-4 m appear in the bay area after we added tsunami data to the inversion. This offshore area is less constrained by the SAR images, and the normal components are required to explain the observed tsunami waves.

The slip amount along the rupture in Figure 9c exhibits two main asperities with slip larger than 9 m between two bends, one at ~1.1°S north of the releasing bend, which was also retrieved by SAR-only inversion, and another in the southern bay area, which was constrained by tsunami data. A small asperity at the south of the epicenter is also presented to explain the surface offsets. The inversion also well reconstructs the observed azimuth offsets in the descending and ascending SAR images. Figure S4 shows the misfits of the azimuth offsets, where the misfits are smaller than 1 m in most of the source area.

The joint inversion model reconstructs well the observed waveform as shown in Figure 6c, which is significantly improved than the SAR-only inversion. The synthetic

tsunami matches well the phase and amplitude of the leading part in the observation. The unusual waveform appeared from 8 to 15 minutes after the earthquake with a 3-m wave (Figure 6c) could be a result of the reflection or nonlinear effects of the bay. The simulated tsunami is much smaller than that observed at Mamuju (Figure S7), where the tsunami may come from another source. Other than the earthquake, a landslide was also considered as a secondary or main source (Carvajal et al. 2019; Gusman et al., 2019; Sassa & Takagawa, 2019). The coseismic vertical deformation is shown in Figure S5.

The nodal plane strike/dip/rake calculated from the joint inversion slip distribution was 352°/64°/-13°, which is very close to the one by SAR-only inversion and compatible with the plane by the Global CMT solution of 348°/57°/-15° (Dziewonski et al., 1981; Ekström et al., 2012) and the USGS W-phase Moment Tensor solution of 350°/67°/-17° by the United States Geological Survey (2018). Although the characteristic focal mechanism shows strike-slip faulting on the fault plane, the local dip-slip components are still able to generate a regional devastating tsunami in Palu bay. The finite-fault parameters of the joint inversion model are provided in Supporting Information.

4.4 Tsunami Inundation

To evaluate the tsunami inundation, we applied the nonlinear SWE to the finest grids Layer 3, which covered the entire coast of Palu bay, as noted in section 3.2. We adopted the slip model inverted by the joint inversion (Figure 7b) as the initial condition. According to the tide prediction of BIG, the tsunami occurred during the high tide, so we considered the sea-level rise for 1 m when computing the flow depth. We divided the coast of Palu bay into three parts by the west, south, and east coasts. The Palu city is located on the south coast. The overall impacts to the coastal communities along the west and east coasts were less severe than the south coast because of the steep topography in those areas on the west and east coasts.

Figure 10a, 11a, and 12a show the estimated flow depth for the south coast (Layer 3-4), west coast (Layer 3-5 to 3-7), and east coast (Layer 3-1 to 3-3), respectively. The estimated flow depth was also compared to the field measurements (Mikami et al., 2019; Paulik et al., 2019) in Figure 10b, 11b, and 12b. We also computed the maximum flow depth on the coastline represented by blue blocks in Figure 10b, 11b, and 12b.

On the south coast, high flow depths were measured near the mouth of Palu River and decreased westward and eastward. Up to 4-m-high flow depths were measured at the two sides of the mouth of Palu River, where we partially reproduced the flow depth by about 1-2 m height at the measuring positions. The measured flow depths reduce to smaller than 2 m on the area further east of the river mouth. We had a good estimation near 119.865°E with ~1 m flow depth. On the west side of the river mouth, we reproduced the flow depths on the coast between 119.84°E and 119.85°E. Further west of 119.84°E, the flow depth increased to up to 5 m, but the estimated flow depth decreased to only 0-2 m high.

Figure 11 shows the result for the west coast. Our model caused up to 5 m flow depth on the coastline, but the inundation distance was so short and we could not reproduce the flow depth at the measured locations. On the east coast shown in Figure 12, we estimated flow depths of higher than 5 m on the coastline between 0.75°S and 0.85°S. Our model induced higher flow depth and longer inundation distance on the east coast than the west coast.

The estimated inundation shows a general pattern similar to the observation that the inundation is stronger on the south coast and weaker on the east and west coasts. Our model reproduces the flow depths in some places on the south coast but underestimates the inundations on the west and east coasts and some parts of the south coast. This result suggests that the general pattern of the tsunami source is reproduced and implies a secondary source to account for the local high flow depths, such as a landslide.

5 Discussion

In the teleseismic source inversion, a simple rectangular fault geometry is applicable. Koketsu et al. (2011) and Yokota et al. (2011) have performed separate and joint inversions utilizing teleseismic, strong motion, geodetic, and/or tsunami data to estimate the source of the 2011 Tohoku earthquake. They exhibited checkerboard resolution tests and real case inversions and pointed out that teleseismic-data-only inversions show limited spatial resolution. Our teleseismic source inversion utilizes low-frequency body and surface waves. The result resolves a characteristic source mechanism with a general slip distribution rather than the details such as small asperities. Thus, a simple rectangular fault geometry is applicable for the teleseismic source inversion. In other words, because teleseismic-data-only inversion is not sensitive to subtle slip variations but resolves a smooth slip model, we can expect a similar inverted slip model if we apply a complex geometry with the same method. However, the induced tsunami by the slip model is controlled by local offshore slip, so a similar slip distribution could induce very different tsunami waves. The source model estimated by the teleseismic source inversion located the major asperity at shallow depth in the bay area and the computed tsunami implied that the observed tsunami waveform can be explained by fault rupture. We then carried out the joint inversion of SAR and tsunami data to estimate the detailed slip distribution.

To estimate a detailed slip distribution, we applied a complex fault geometry for the joint inversion and the SAR-only inversion. The offsets in different directions recorded by SAR images revealed a clear rupture trace that allowed us to determine a complex fault geometry, which was appropriate for the SAR-only inversion and joint inversion to retrieve a detailed slip distribution. Due to the clear boundary of offsets of different directions, if we apply a simple geometry to the SAR-only or joint inversion, we will fail to fit the offsets somewhere, e.g., the bend areas. The SAR images have no contribution to the bay (sea) area, where the offshore slip is only constrained by the adjacent land offset records in SAR-only inversion. In contrast, tsunami waves, which are induced by offshore displacement, provide good constraints for the offshore area. By adding tsunami data to the inversion, we can retrieve the slip distribution that generates the observed tsunami waveform. Although the SAR images dominated the joint inversion because they recorded the land offsets of most of the rupture area, the tsunami data still provide an important contribution to the offshore slip. Figure 7 exhibits noticeable slip differences in the bay area that indicates the indispensable contribution of tsunami data to the joint inversion.

Our inversion results are comparable to other studies in some parts. Our SAR-only inverted model exhibits weak oblique slip near the retraining and releasing bends, which is comparable to the results of Socquet et al. (2019) and He et al. (2019). Socquet et al. (2019) estimated oblique slip with comparable strike-slip and dip-slip components in the bay area and the releasing bend at 1.2°S and 0.2°S. He et al. (2019) had a similar source model on their onshore segments. The restraining bend area is located in the bay area, where different slip was retrieved. Our joint inversion model retrieved normal slip near the bay, which were

also estimated by Ulrich et al. (2019), who addressed a regional releasing beneath the bay and retrieved 2-m normal slip in the bay area, and Fang et al. (2019) also estimated normal slip up to 2 m in Palu bay. Lee et al. (2019) estimated an oblique-to-normal slip from the epicenter to the bay at a ~15 km depth.

An offshore normal fault based on the bathymetry was added by Song et al. (2019) and He et al. (2019). According to Song et al. (2019), the additional normal fault improved the misfit of InSAR data for the northwest island further north of 0.3°S. The inverted slip distribution is identical to the one without an additional segment in the area further south of 0.5°S. Although they claimed that the normal fault may be the source of the tsunami, the northwest offshore segment is too far to be the source for the leading tsunami wave. However, the predicted tsunami at Mamuju may be improved by an offshore segment.

The observed tsunami wave was neither explained by the strike-slip displacement (Lee et al., 2019), the oblique slip (Socquet et al., 2019), nor an additional offshore normal-faulting segment (Song et al. 2019). Ulrich et al. (2019) retrieved normal slip in the bay area and their model reproduced the magnitude of the tsunami wave. Our joint inversion source model reconstructed the tsunami waveform at Pantoloan and the flow depths in some areas on the south coast, but failed to reproduce the local high flow depth in other places. The underestimation can be contributed by some factors, for example, the precision of measuring positions, accuracy of topographic data, the inverted model, and additional sources. The error of measuring position can result from device error and inherent positioning error of different signal conditions, but it can only explain some specific positions.

The accuracy and precision of the topographic data can be discussed separately. The topographic data, which was provided by BIG, should be accurate for tsunami inundation computation, but the DEM does not include the urban land cover, e.g., buildings and streets, which could generate estimation errors. According to the study of Ali et al. (2015), DEMs in different resolutions did not show significant differences in flood assessment. The quality and accuracy of a DEM are more important than the resolution and precision. Savage et al. (2016) demonstrated that the performance of deterministic simulations degrades as resolution coarser than 50 m, and has little improvement when resolution finer than 50 m. We applied the high-resolution bathymetric contour and topographic data from BIG to construct our Layer 2 and Layer 3, where the Layer 3 has the finest resolution of 20 m (east-west direction) by 13 m (north-south direction). Although the buildings and streets are not included on top of the topography in the DEM, the resolution should be applicable to approximately estimate the inundation for source assessment. Future work to explore the detailed flood in the city should consider the urban land cover.

Since we reconstructed well the tsunami wave at Pantoloan and partially reproduced the flow depth of the south coast, the characteristic pattern of the tsunami should be retrieved by our source model. A secondary source is a reasonable explanation for the local high flow depths. Although landslide events were suggested by previous studies (Carvajal et al., 2019; Gusman et al., 2019; Sassa & Takagawa, 2019), the precise location and dimension are still controversial. Future investigation and exploration will provide more evidence and uncover the puzzle.

6 Conclusions

To examine if the tsunami can be induced by the rupture displacements, we performed a two-step analysis of the 2018 Palu earthquake by performing two inversion methods with two different data sets: step one, the teleseismic source inversion, and step two, the SAR-only inversion and the joint inversion of SAR and tsunami data.

Our teleseismic source inversion indicated that a strike-slip rupture propagated from the hypocenter to the south, with the major asperity located at about 50 km south of the hypocenter in the shallow part. The observed tsunami waveform at Pantoloan was explained by the slip distribution, suggesting that the strike-slip faulting with localized dip-slip was the major cause of the tsunami. We then estimated the fault slip distribution with only SAR data, but the computed tsunami could not reproduce the observed tsunami waveform, because the offshore slip was not well resolved. The joint inversion of SAR and tsunami data shows a strike-slip fault which consists of three segments extending from the epicenter to the south of 1.4°S with two bends and two asperities around Palu city. The tsunami data provides necessary information to reconstruct the slip distribution inside the bay that reproduces well the observed tsunami waveform at Pantoloan and part of inundations in Palu city. However, to fully explain the high inundations near Palu bay, additional sources, such as landslides, are also suggested. We provide the parameters for the finite faults of the joint inversion in the supporting information Dataset S1.

Finally, this study points out that local devastating tsunamis can result from a strike-slip fault. This suggests that offshore and/or onshore strike-slip faults should be considered in tsunami hazard assessment to account for regional tsunamis.

Acknowledgement

The Copernicus Sentinel data (Sentinel-1) are provided from the European Space Agency (ESA). The tide gauge data at Pantoloan station are from the Geospatial Information Agency of Indonesia (Badan Informasi Geospasial, BIG) http://tides.big.go.id/. The DEMNAS and BATNAS topographic and bathymetric datasets are downloaded from the Geospatial Information Agency of Indonesia (BIG) http://tides.big.go.id/. Earthquake Catalog courtesy of the U.S. Geological Survey. The authors appreciate the valuable suggestions from Drs. Yuichiro Tanioka and Nobuhito Mori. This work was supported by JST J-RAPID JPMJJR1805, by KAKENHI (16H01838 19K04034), and by Core-to-Core Collaborative research program of the Earthquake Research Institute, The University of Tokyo and the Disaster Prevention Research Institute, Kyoto University. The authors appreciate the valuable comments and suggestions from the two anonymous reviewers.

Reference

Aki, K., & Richards, P. G. (2002). *Quantitative seismology, 2nd Ed*. University Science Books.

Ali, A. M., Solomatine, D. P., & Di Baldassarre, G. (2015). Assessing the impact of different sources of topographic data on 1-D hydraulic modelling of floods. Hydrology and Earth System Sciences, 19(1), 631-643.

Baba, T., Takahashi, N., Kaneda, Y., Ando, K., Matsuoka, D., & Kato, T. (2015). Parallel implementation of dispersive tsunami wave modeling with a nesting algorithm for the 2011 Tohoku tsunami. Pure and Applied Geophysics, 172(12), 3455-3472. http://doi.org/10.1007/s00024-015-1049-2

Bao, H., Ampuero, J. P., Meng, L., Fielding, E. J., Liang, C., Milliner, C. W., ... & Huang, H. (2019). Early and persistent supershear rupture of the 2018 magnitude 7.5 Palu earthquake. Nature Geoscience DOI, 10. https://doi.org/10.1038/s41561-018-0297-z

Bassin, C., G. Laske, and G. Masters (2000). The current limits of resolution for surface wave tomography in North America. Eos, Transactions of the American Geophysical Union, 81, F897 (http://igppweb.ucsd.edu/~gabi/crust2.html).

Carvajal, M., Araya-Cornejo, C., Sepúlveda, I., Melnick, D., & Haase, J. S. (2019). Nearly instantaneous tsunamis following the Mw 7.5 2018 Palu earthquake. Geophysical Research Letters, 46. https://doi.org/10.1029/2019GL082578

Dziewonski, A. M. and D. L. Anderson (1981). Preliminary reference Earth model. Phys. Earth Planet. Inter. 25(4), 297–356.

Dziewonski, A. M., Chou, T. A., & Woodhouse, J. H. (1981). Determination of earthquake source parameters from waveform data for studies of global and regional seismicity. Journal of Geophysical Research: Solid Earth, 86(B4), 2825-2852. https://doi.org/10.1029/JB086iB04p02825

Ekström, G., Nettles, M., & Dziewoński, A. M. (2012). The global CMT project 2004–2010: Centroid-moment tensors for 13,017 earthquakes. Physics of the Earth and Planetary Interiors, 200, 1-9. https://doi.org/10.1016/j.pepi.2012.04.002

Fang, J., Xu, C., Wen, Y., Wang, S., Xu, G., Zhao, Y., & Yi, L. (2019). The 2018 Mw 7.5 Palu Earthquake: A Supershear Rupture Event Constrained by InSAR and Broadband Regional Seismograms. Remote Sensing, 11(11), 1330.

Gusman, A. R., Supendi, P., Nugraha, A. D., Power, W., Latief, H., Sunendar, H., ... & Wang, X. (2019). Source model for the tsunami inside Palu Bay following the 2018 Palu earthquake, Indonesia. Geophysical Research Letters, 46(15), 8721-8730. http://dx.doi.org/10.1029/2019GL082717

He, L., Feng, G., Li, Z., Feng, Z., Gao, H., & Wu, X. (2019). Source parameters and slip distribution of the 2018 Mw 7.5 Palu, Indonesia earthquake estimated from space-based geodesy. Tectonophysics, 772, 228216. https://doi.org/10.1016/j.tecto.2019.228216

Heidarzadeh, M., Muhari, A., & Wijanarto, A. B. (2019). Insights on the source of the 28 September 2018 Sulawesi tsunami, Indonesia based on spectral analyses and numerical simulations. Pure and Applied Geophysics, 176(1), 25-43. https://doi.org/10.1007/s00024-018-2065-9

Ho, T. C., Satake, K., & Watada, S. (2017). Improved phase corrections for transoceanic tsunami data in spatial and temporal source estimation: Application to the 2011 tohoku earthquake. Journal of Geophysical Research: Solid Earth, 122(12), 10-155. https://doi.org/10.1002/2017JB015070

Ho, T. C., Satake, K., Watada, S., & Fujii, Y. (2019). Source estimate for the 1960 chile earthquake from joint inversion of geodetic and transoceanic tsunami data. Journal of Geophysical Research: Solid Earth, 124(3), 2812-2828. https://doi.org/10.1029/2018JB016996

Ji, C., Wald, D. J., & Helmberger, D. V. (2002). Source description of the 1999 Hector Mine, California, earthquake, part I: Wavelet domain inversion theory and resolution analysis. Bulletin of the Seismological Society of America, 92(4), 1192-1207.

Koketsu, K., Yokota, Y., Nishimura, N., Yagi, Y., Miyazaki, S. I., Satake, K., ... & Okada, T. (2011). A unified source model for the 2011 Tohoku earthquake. Earth and Planetary Science Letters, 310(3-4), 480-487. https://doi.org/10.1016/j.epsl.2011.09.009

Lee, S. J., Wong, T. P., Lin, T. C., & Liu, T. Y. (2019). Complex Triggering Supershear Rupture of the 2018 M w 7.5 Palu, Indonesia, Earthquake Determined from Teleseismic Source Inversion. Seismological Research Letters.

Michel, R., Avouac, J. P., and Taboury, J. (1999) Measuring ground displacements from SAR amplitude images: application to the Landers earthquake. Geophysical Research Letters, 26, 875-878. http://doi.org/10.1029/1999GL900138.

Mikami, T., Shibayama, T., Esteban, M., Takabatake, T., Nakamura, R., Nishida, Y., ... & Krautwald, C. (2019). Field survey of the 2018 Sulawesi tsunami: inundation and run-up heights and damage to coastal communities. Pure and Applied Geophysics, 176(8), 3291-3304. https://doi.org/10.1007/s00024-019-02258-5

Muhari, A., Imamura, F., Arikawa, T., Hakim, A. R., & Afriyanto, B. (2018). Solving the puzzle of the September 2018 pale, Indonesia, tsunami mystery: Clues from the tsunami waveform and the initial field survey data. Journal of Disaster Research, 13, sc20181108. https://doi.org/10.20965/jdr.2018.sc20181108

Okada, Y. (1985). Surface deformation due to shear and tensile faults in a half-space. Bulletin of the seismological society of America, 75(4), 1135-1154.

Omira, R., Dogan, G. G., Hidayat, R., Husrin, S., Prasetya, G., Annunziato, A., ... & Zaytsev, A. (2019). The September 28th, 2018, Tsunami In Palu-Sulawesi, Indonesia: A Post-Event Field Survey. Pure and Applied Geophysics, 176(4), 1379-1395. https://doi.org/10.1007/s00024-019-02145-z

Paulik, R., Gusman, A., Williams, J. H., Pratama, G. M., Lin, S. L., Prawirabhakti, A., ... & Suwarni, N. W. I. Tsunami Hazard and Built Environment Damage Observations from Palu City after the September 28 2018 Sulawesi Earthquake and Tsunami. Pure and Applied Geophysics, 1-17.

Prasetya, G. S., De Lange, W. P., & Healy, T. R. (2001). The makassar strait tsunamigenic region, Indonesia. Natural Hazards, 24(3), 295-307.

Rothman, D. H. (1986). Automatic estimation of large residual statics corrections. Geophysics, 51(2), 332-346.

Sassa, S., & Takagawa, T. (2019). Liquefied gravity flow-induced tsunami: First evidence and comparison from the 2018 Indonesia Sulawesi earthquake and tsunami disasters. Landslides, 16(1), 195–200. https://doi.org/10.1007/s10346-018-1114-x

Satake, K., Fujii, Y., Harada, T., & Namegaya, Y. (2013). Time and space distribution of coseismic slip of the 2011 Tohoku earthquake as inferred from tsunami waveform data. Bulletin of the seismological society of America, 103(2B), 1473-1492.

Savage, J. T. S., Bates, P., Freer, J., Neal, J., & Aronica, G. (2016). When does spatial resolution become spurious in probabilistic flood inundation predictions?. Hydrological Processes, 30(13), 2014-2032.

Socquet, A., Simons, W., Vigny, C., McCaffrey, R., Subarya, C., Sarsito, D., ... & Spakman, W. (2006). Microblock rotations and fault coupling in SE Asia triple junction (Sulawesi, Indonesia) from GPS and earthquake slip vector data. Journal of Geophysical Research: Solid Earth, 111(B8).

Socquet, A., Hollingsworth, J., Pathier, E., & Bouchon, M. (2019). Evidence of supershear during the 2018 magnitude 7.5 Palu earthquake from space geodesy. Nature Geoscience, 12(3), 192. https://doi.org/10.1038/s41561-018-0296-0

618 Song, X., Zhang, Y., Shan, X., Liu, Y., Gong, W., & Qu, C. (2019). Geodetic observations of
619 the 2018 Mw 7.5 Sulawesi earthquake and its implications for the kinematics of the
620 Palu fault. Geophysical Research Letters, 46(8), 4212-4220.

621 Tanioka, Y., & Satake, K. (1996). Tsunami generation by horizontal displacement of ocean
622 bottom. Geophysical Research Letters, 23(8), 861-864.

623 Ulrich, T., Vater, S., Madden, E. H., Behrens, J., van Dinther, Y., Van Zelst, I., ... & Gabriel,
624 A. A. (2019). Coupled, physics-based modeling reveals earthquake displacements are
625 critical to the 2018 Palu, Sulawesi Tsunami. Pure and Applied Geophysics, 176(10),
626 4069-4109.

627 United States Geological Survey (2018). M7.5—70 km No of Palu Indonesia,
628 https://earthquake.usgs.gov/earthquakes/eventpage/us1000h3p4/executive

629 Watada, S., Kusumoto, S., & Satake, K. (2014). Traveltime delay and initial phase reversal of
630 distant tsunamis coupled with the self-gravitating elastic Earth. Journal of
631 Geophysical Research: Solid Earth, 119(5), 4287-4310.
632 https://doi.org/10.1002/2013JB010841

633 Wright, P., Macklin, T., Willis, C., & Rye, T. (2005). Coherent change detection with SAR.
634 In European Radar Conference, 2005. EURAD 2005. (pp. 17-20). IEEE.

635 Yokota, Y., Koketsu, K., Fujii, Y., Satake, K., Sakai, S. I., Shinohara, M., & Kanazawa, T.
636 (2011). Joint inversion of strong motion, teleseismic, geodetic, and tsunami datasets
637 for the rupture process of the 2011 Tohoku earthquake. Geophysical Research Letters,
638 38(7). https://doi.org/10.1029/2011GL050098

639 Yolsal-Çevikbilen, S., & Taymaz, T. (2019). Source Characteristics of the 28 September
640 2018 Mw 7.5 Palu-Sulawesi, Indonesia (SE Asia) Earthquake Based on Inversion of
641 Teleseismic Bodywaves. Pure and Applied Geophysics, 1-16.

642 Yalciner A. C. et al. (2018). The 28th September 2018 Palu Earthquake and Tsunami ITST,
643 07-11 November 2018 Post Tsunami Field Survey Report (Short).

644

645

646 **Figure 1.** The three layers for computing the tsunami waveforms and inundations. (a) The
647 entire computational domain of Layer 1 and the region of Layer 2. The Red star indicates the
648 epicenter, and the white circles show the aftershocks of M4.0 to M5.9 within two months
649 after the mainshock provided by the USGS Earthquake Catalog. (b) The domain of Layer 2
650 and the seven black rectangles indicate the areas of Layer 3 where the numbers from 1 to 7 at
651 the southeast corner represent the Layer 3-1 to 3-7. The blue inverted triangle indicates the
652 tide gauge at Pantoloan. The magenta dots show the locations of inundation/flow depth
653 observations.

654

655 **Figure 2.** Azimuth offsets from (a) descending (S20°W) and (b) ascending (N20°W) images
656 observed by Sentinel-1. The red stars show the epicenter of the earthquake. The black and
657 green arrows indicate the azimuth and range directions, respectively.

658

Figure 3. The tsunami waveform recorded by the Pantoloan tide gauge. (a) shows the raw data, (b) is the de-tided waveform. The red-shaded window shows the signals used in the inversions.

Figure 4. Waveform comparisons between observed (black) and synthetic (red) (a) teleseismic body waves and (b) teleseismic surface waves. In each panel, station and phase IDs are labeled on the left. Phase IDs are abbreviated as follows: 'P' for P wave, 'SH' for SH wave, 'RA' for Rayleigh wave, and 'LO' for Love wave, respectively. The numbers above and below the beginning of each trace indicate azimuth relative to the source and epicentral distance, both in degrees. The observed peak ground displacement in micrometers is shown at the end of each trace.

Figure 5. The slip distribution of the Palu earthquake in (a) map view and (b) cross-section. The gray star denotes the hypocenter. In (a) and (b), the background color on the fault plane indicates the amount of slip. In (b), the rake angle is indicated by the arrow at each subfault center. The contours represent the elapsed time the rupture from its onset in seconds with a contour interval of 5 s.

Figure 6. Waveform comparisons between the observed and calculated waveforms by (a) the teleseismic inversion, (b) the SAR-only inversion, and (c) the joint inversion model. The blue-shaded windows indicate the data used in our inversion.

Figure 7. Slip distributions derived from (a) the source inversions with only SAR images and (b) the joint inversion with SAR and tsunami data. Color and arrows indicate the slip amplitude and the rake angle, respectively. The star denotes the epicenter.

Figure 8. Slip distribution of (a) dip-slip and (b) strike-slip components, and (c) slip amount estimated by SAR-only inversion. Negative indicates the reverse-faulting component in (a). S-Bend represents the releasing bend and N-bend indicates the restraining bend. The star indicates the hypocenter.

Figure 9. Slip distribution of (a) dip-slip and (b) strike-slip components, and (c) slip amount estimated by joint inversion.

Figure 10. The estimated flow depth on the south coast of Palu bay in Layer 3-4. (a) The computed flow depth is shown in color. Dark crosses indicate the measuring positions of field surveys. (b) The observed (dark crosses) and computed (red circles) flow depth at measuring positions of field surveys. The blue blocks represent the computed maximum flow depths on the coastline.

Figure 11. The estimated flow depth on the west coast of Palu bay for Layer 3-5 to 3-7. (a) Dark crosses indicate the measuring positions of field surveys. (b) The dark crosses show the

observed flow depth at measuring positions of field surveys. The blue blocks represent the computed maximum flow depths on the coastline.

Figure 12. The estimated flow depth on the east coast of Palu bay for Layer 3-1 to 3-3. (a) Dark crosses indicate the measuring positions of field surveys. (b) The dark crosses show the observed flow depth at measuring positions of field surveys. The blue blocks represent the computed maximum flow depths on the coastline.

Figure 1.

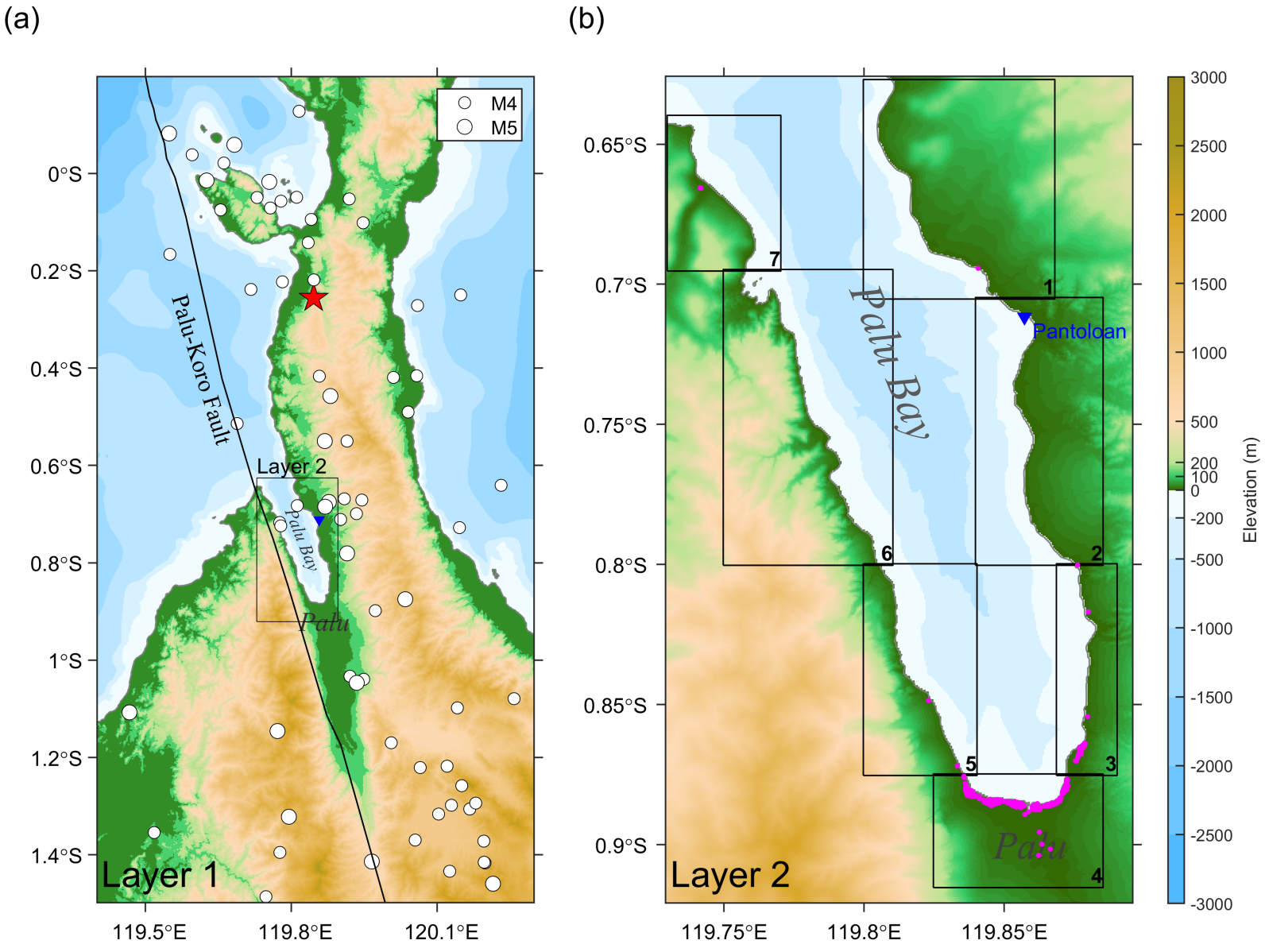
(a)
(b)
M4
M5
Palu-Koro Fault
Layer 2
Palu Bay
Palu
Layer 1
0°S
0.2°S
0.4°S
0.6°S
0.8°S
1°S
1.2°S
1.4°S
119.5°E
119.8°E
120.1°E
0.65°S
0.7°S
0.75°S
0.8°S
0.85°S
0.9°S
119.75°E
119.8°E
119.85°E
Pantoloan
1
2
3
4
5
6
7
Elevation (m)
3000
2500
2000
1500
1000
500
200
100
0
-200
-500
-1000
-1500
-2000
-2500
-3000

Figure 2.

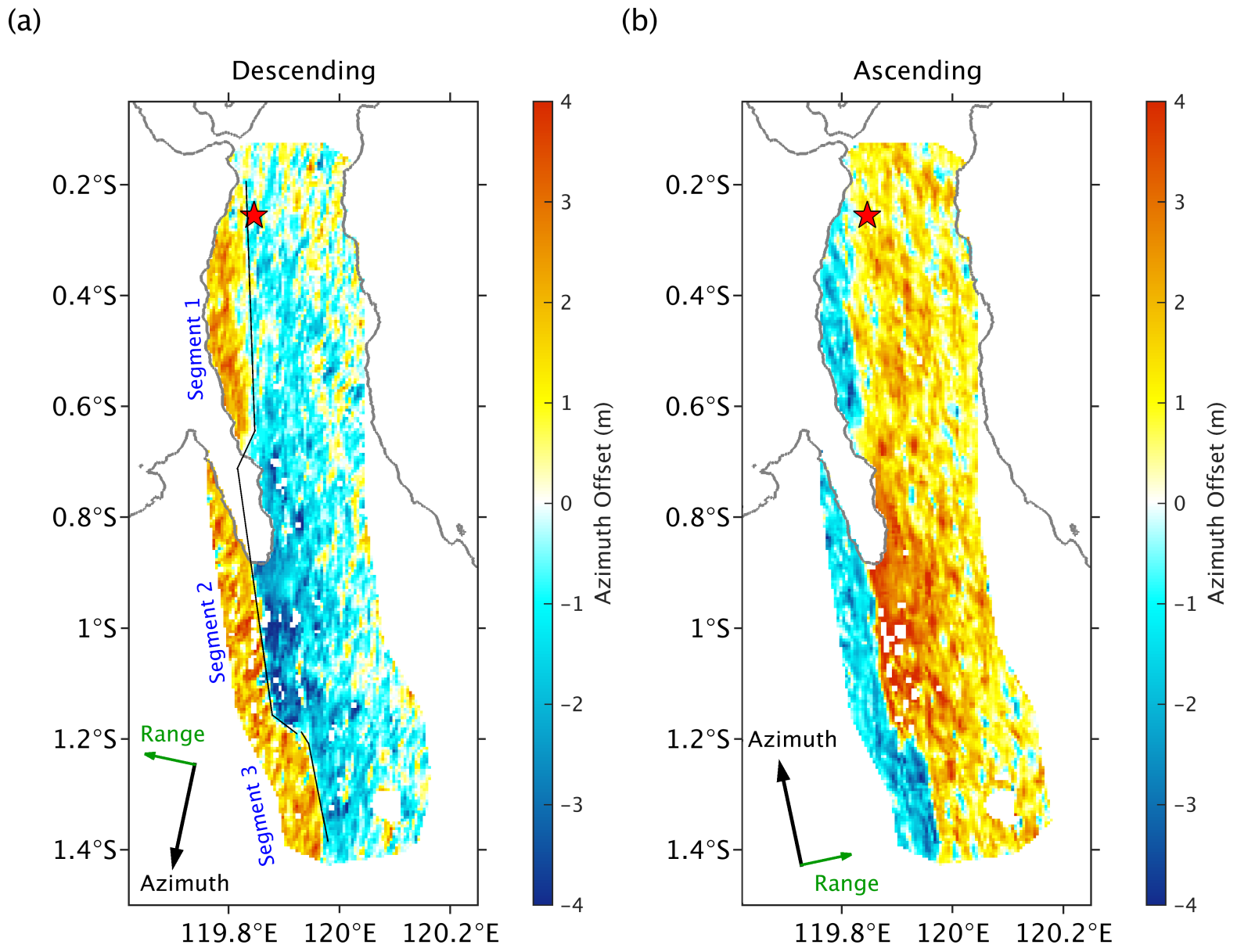
(a)
Descending
0.2°S
0.4°S
0.6°S
0.8°S
1°S
1.2°S
1.4°S
119.8°E
120°E
120.2°E
Segment 1
Segment 2
Segment 3
Range
Azimuth
4
3
2
1
0
−1
−2
−3
−4
Azimuth Offset (m)
(b)
Ascending
0.2°S
0.4°S
0.6°S
0.8°S
1°S
1.2°S
1.4°S
119.8°E
120°E
120.2°E
Azimuth
Range
4
3
2
1
0
−1
−2
−3
−4
Azimuth Offset (m)

Figure 3.

(a)

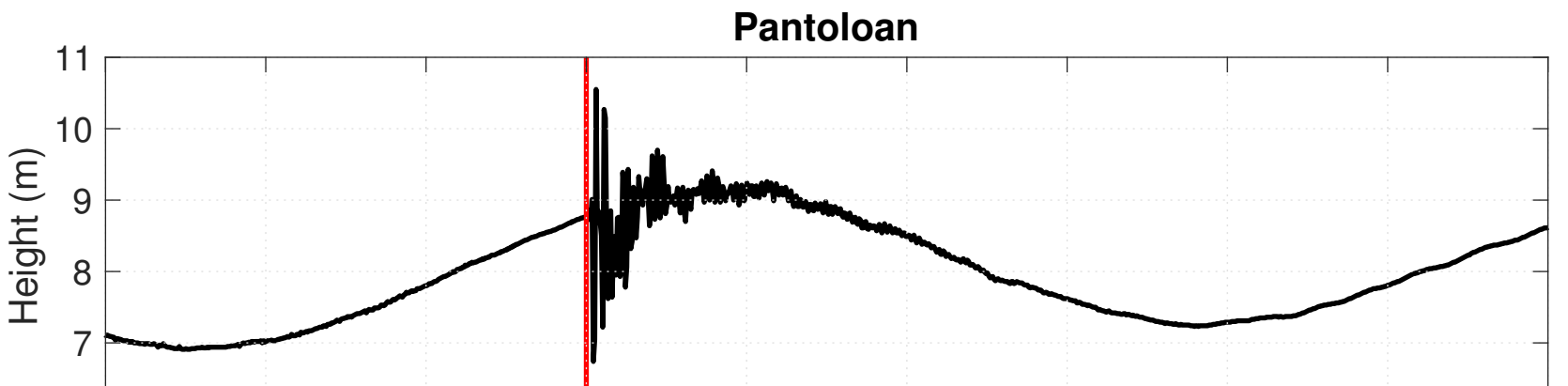
Pantoloan
Height (m)
11
10
9
8
7
6
-6
-4
-2
0
2
4
6
8
10
12
Origin Time (hr)

(b)

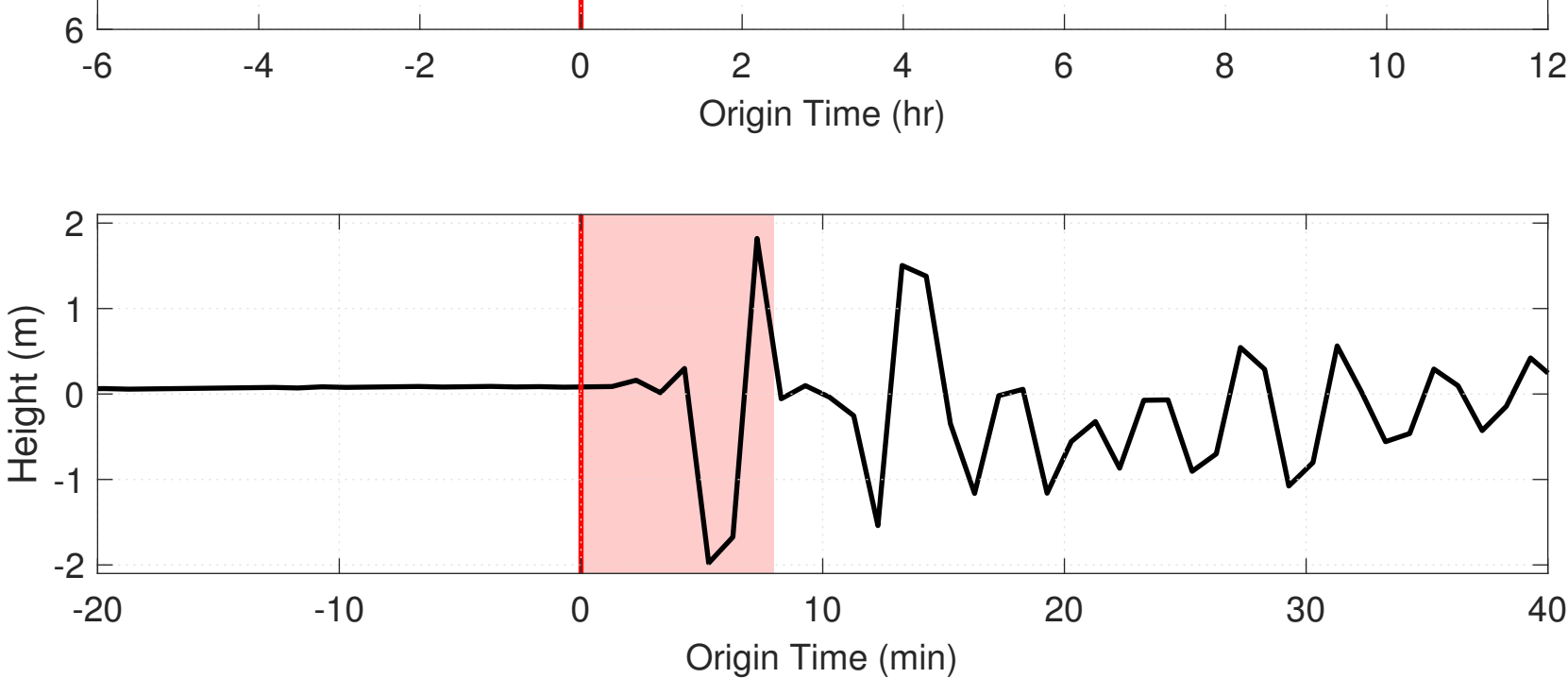
Height (m)
2
1
0
-1
-2
-20
-10
0
10
20
30
40
Origin Time (min)

Figure 4.

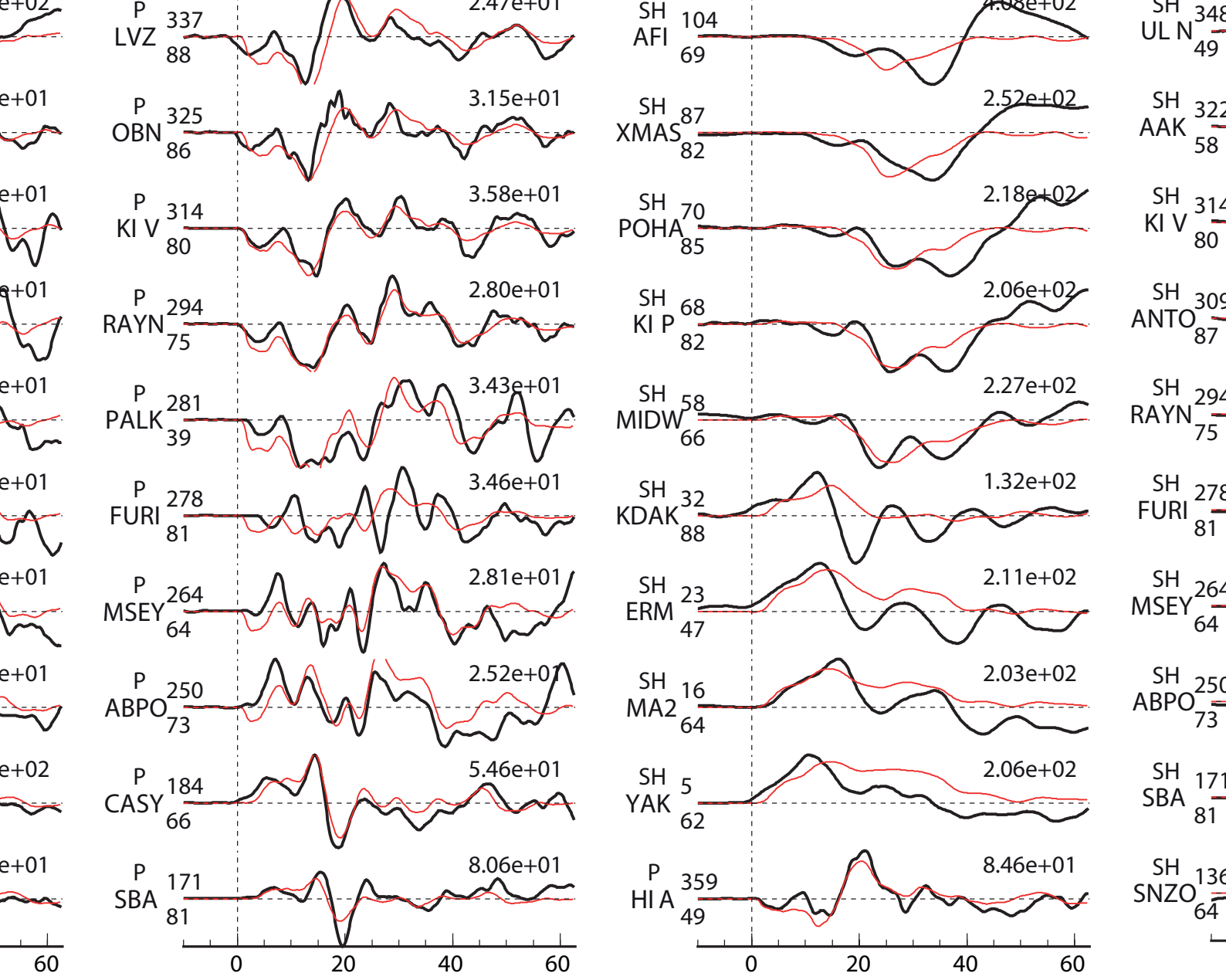
P LVZ 337 88 2.47e+01
P OBN 325 86 3.15e+01
P KI V 314 80 3.58e+01
P RAYN 294 75 2.80e+01
P PALK 281 39 3.43e+01
P FURI 278 81 3.46e+01
P MSEY 264 64 2.81e+01
P ABPO 250 73 2.52e+01
P CASY 184 66 5.46e+01
P SBA 171 81 8.06e+01
SH AFI 104 69
SH XMAS 87 82 2.52e+02
SH POHA 70 85 2.18e+02
SH KI P 68 82 2.06e+02
SH MIDW 58 66 2.27e+02
SH KDAK 32 88 1.32e+02
SH ERM 23 47 2.11e+02
SH MA2 16 64 2.03e+02
SH YAK 5 62 2.06e+02
P HI A 359 49 8.46e+01
SH UL N 348 49
SH AAK 322 58
SH KI V 314 80
SH ANTO 309 87
SH RAYN 294 75
SH FURI 278 81
SH MSEY 264 64
SH ABPO 250 73
SH SBA 171 81
SH SNZO 136 64
0 20 40 60

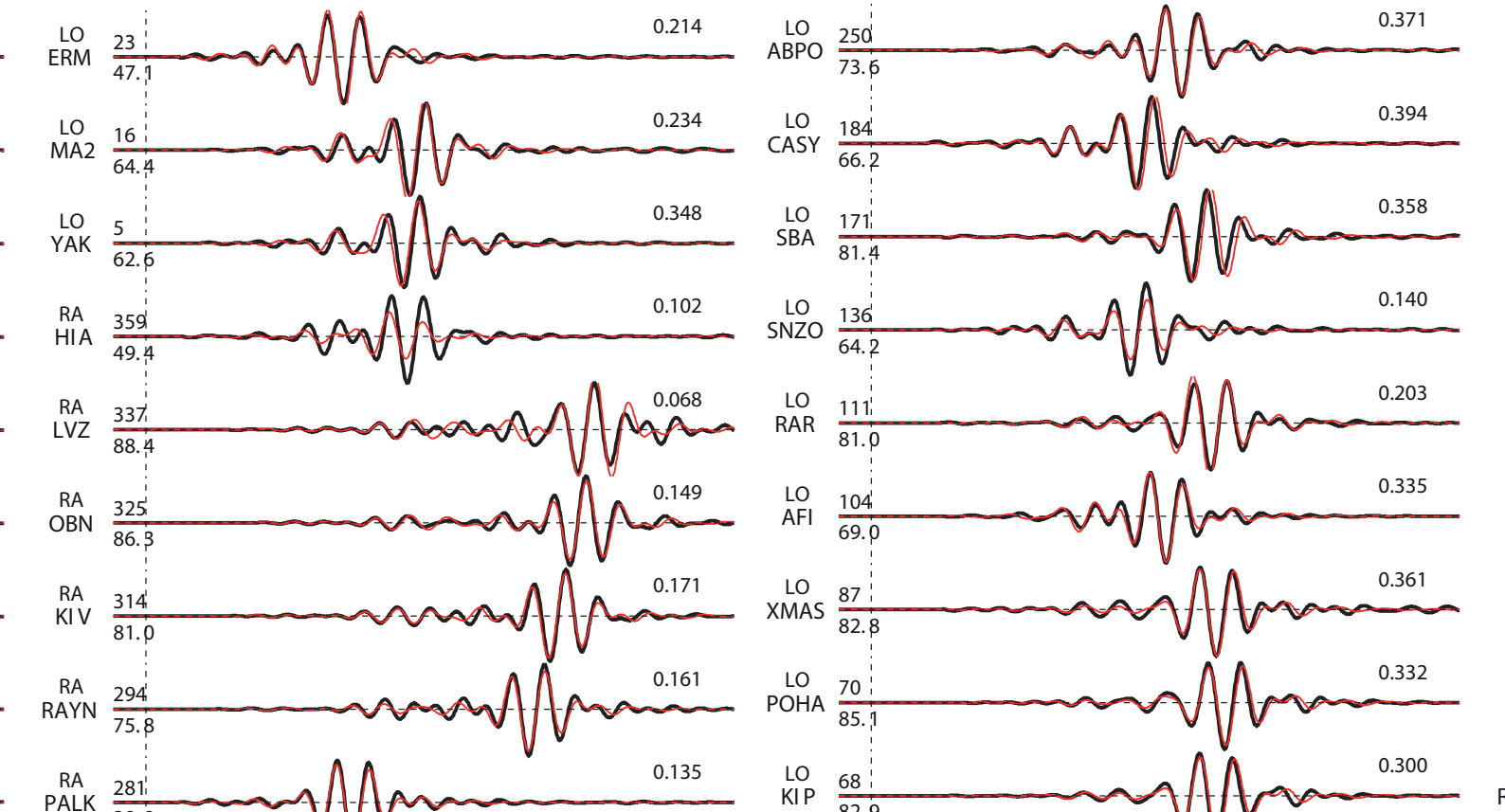
LO ERM 23 47.1 0.214
LO MA2 16 64.4 0.234
LO YAK 5 62.6 0.348
RA HI A 359 49.4 0.102
RA LVZ 337 88.4 0.068
RA OBN 325 86.3 0.149
RA KI V 314 81.0 0.171
RA RAYN 294 75.8 0.161
RA PALK 281 0.135
LO ABPO 250 73.6 0.371
LO CASY 184 66.2 0.394
LO SBA 171 81.4 0.358
LO SNZO 136 64.2 0.140
LO RAR 111 81.0 0.203
LO AFI 104 69.0 0.335
LO XMAS 87 82.8 0.361
LO POHA 70 85.1 0.332
LO KI P 68 0.300

Figure 5.

(a)

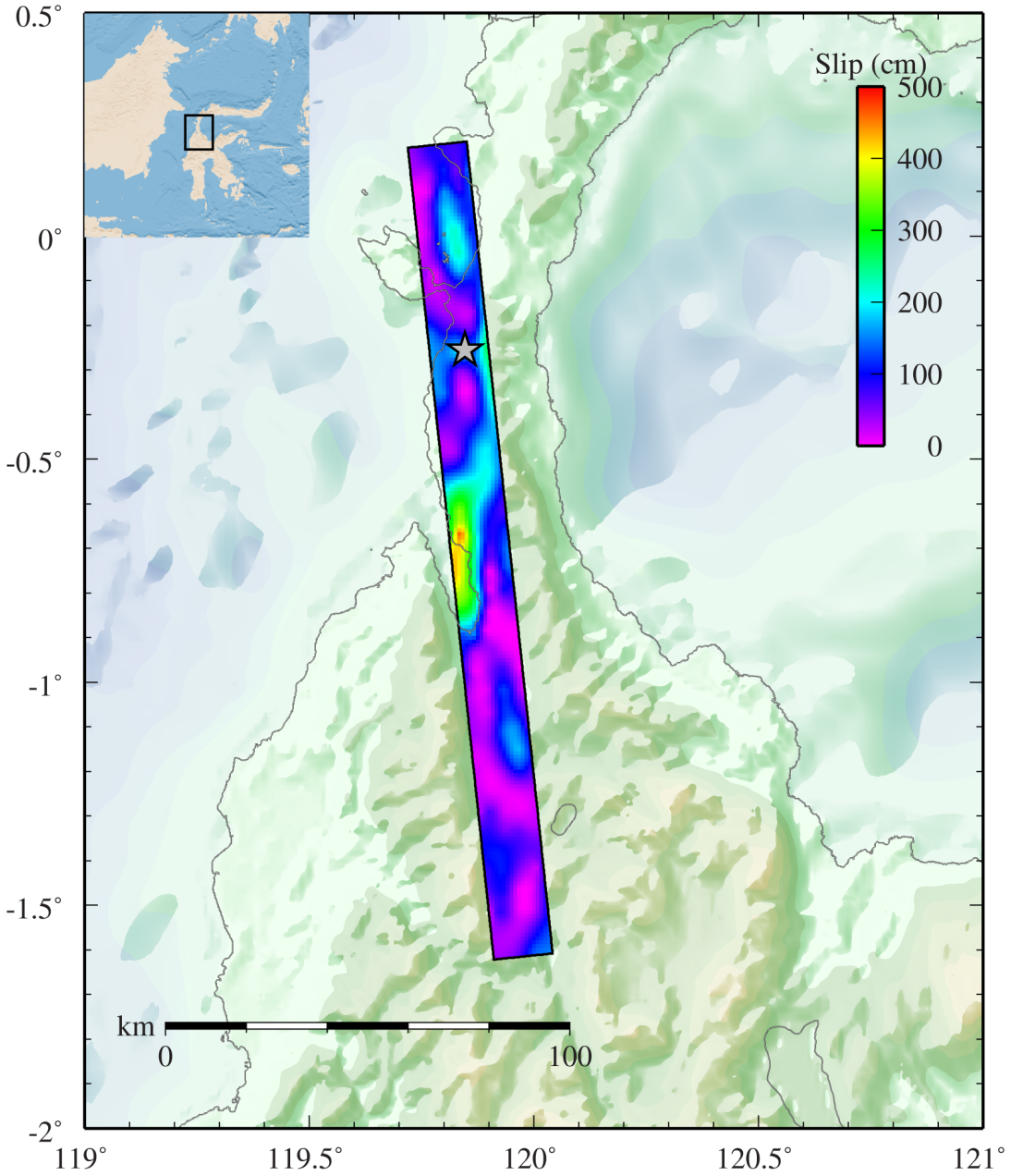
Slip (cm)
500
400
300
200
100
0
0.5°
0°
-0.5°
-1°
-1.5°
-2°
119°
119.5°
120°
120.5°
121°
km
0
100

(b)

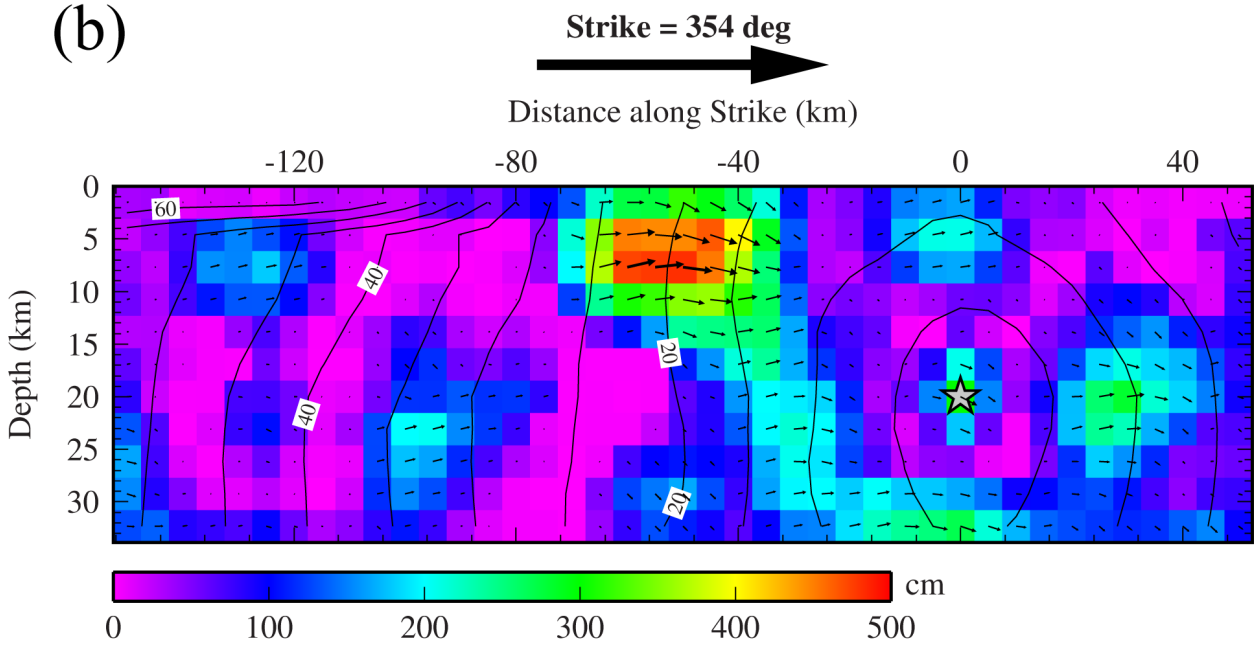
Strike = 354 deg
Distance along Strike (km)
-120
-80
-40
0
40
Depth (km)
0
5
10
15
20
25
30
60
40
40
20
20
cm
0
100
200
300
400
500

Figure 6.

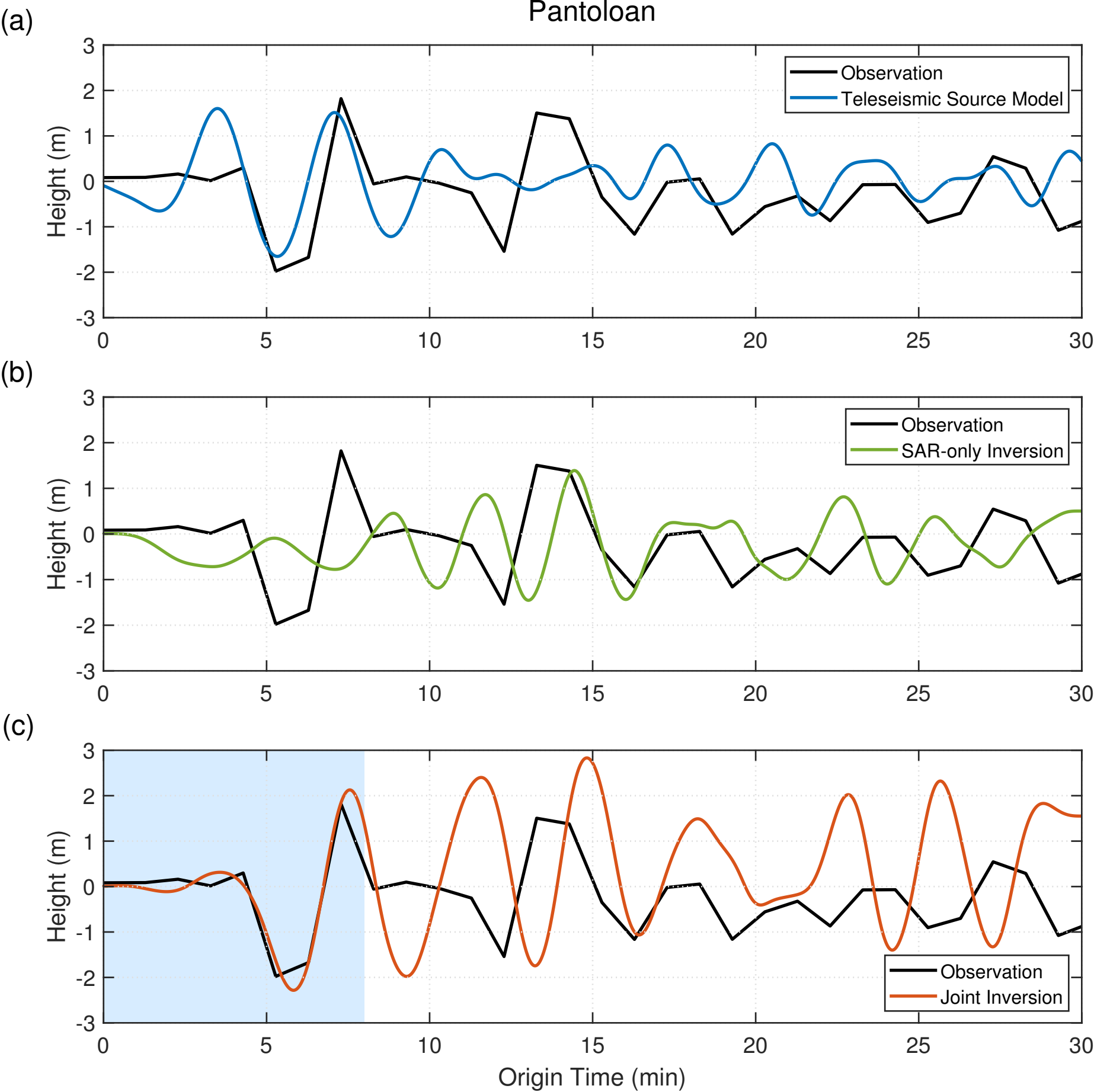
Pantoloan
(a)
Observation
Teleseismic Source Model
Height (m)
(b)
Observation
SAR-only Inversion
Height (m)
(c)
Observation
Joint Inversion
Height (m)
Origin Time (min)

Figure 7.

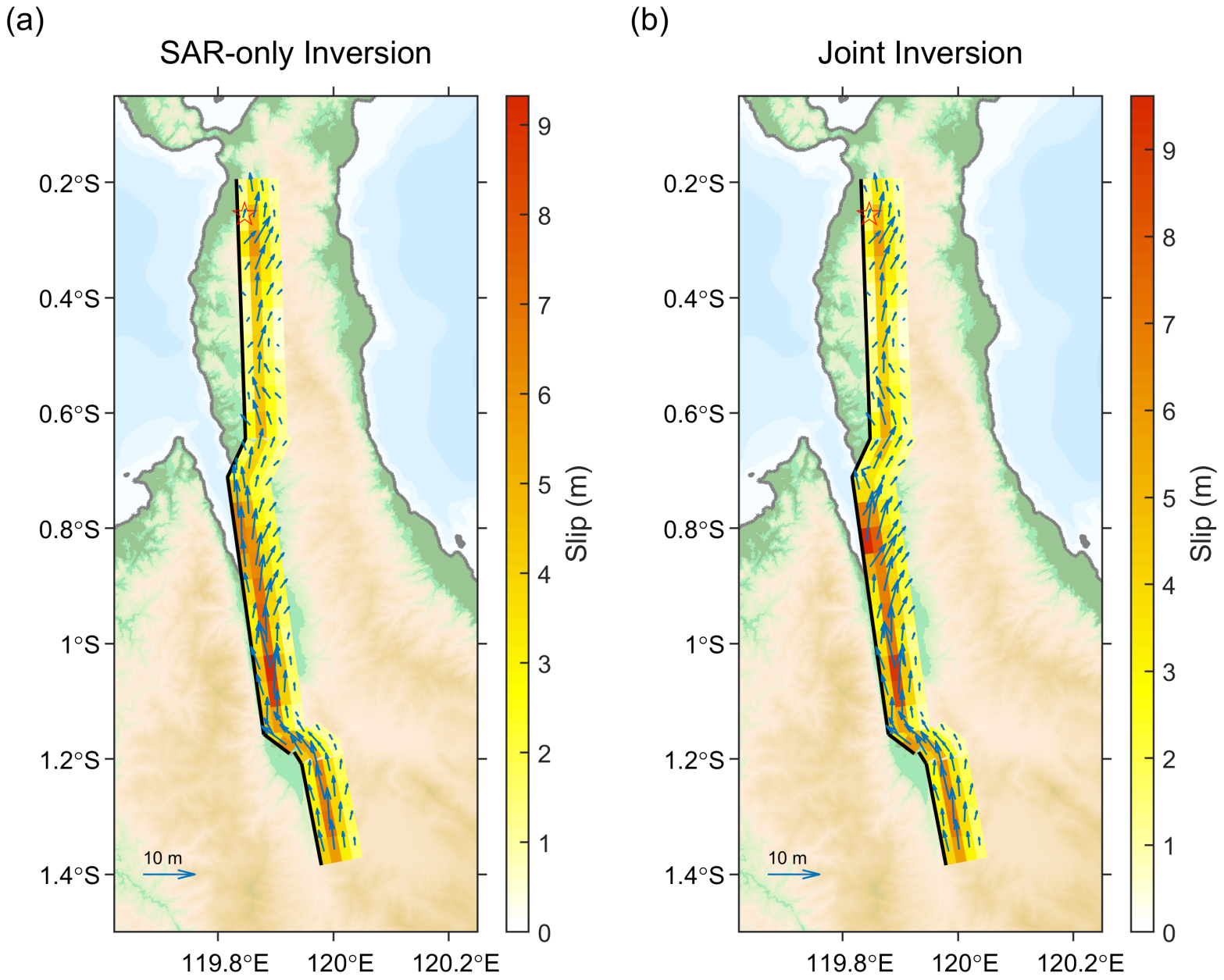
(a)
SAR-only Inversion
(b)
Joint Inversion
0.2°S
0.4°S
0.6°S
0.8°S
1°S
1.2°S
1.4°S
119.8°E
120°E
120.2°E
10 m
Slip (m)
0
1
2
3
4
5
6
7
8
9

Figure 8.

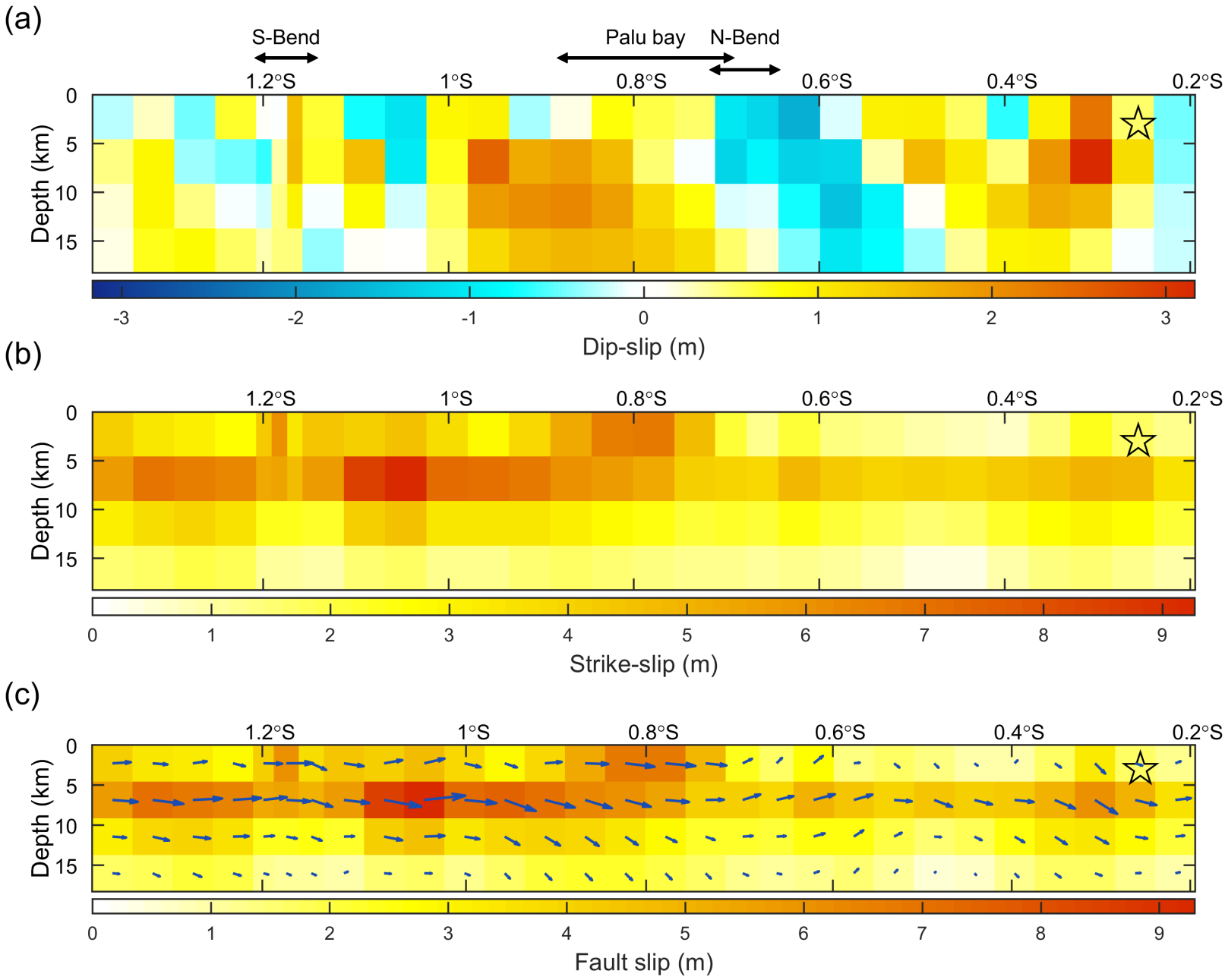
(a)
S-Bend
Palu bay
N-Bend
1.2°S
1°S
0.8°S
0.6°S
0.4°S
0.2°S
Depth (km)
0
5
10
15
-3
-2
-1
0
1
2
3
Dip-slip (m)
(b)
1.2°S
1°S
0.8°S
0.6°S
0.4°S
0.2°S
Depth (km)
0
5
10
15
0
1
2
3
4
5
6
7
8
9
Strike-slip (m)
(c)
1.2°S
1°S
0.8°S
0.6°S
0.4°S
0.2°S
Depth (km)
0
5
10
15
0
1
2
3
4
5
6
7
8
9
Fault slip (m)

Figure 9.

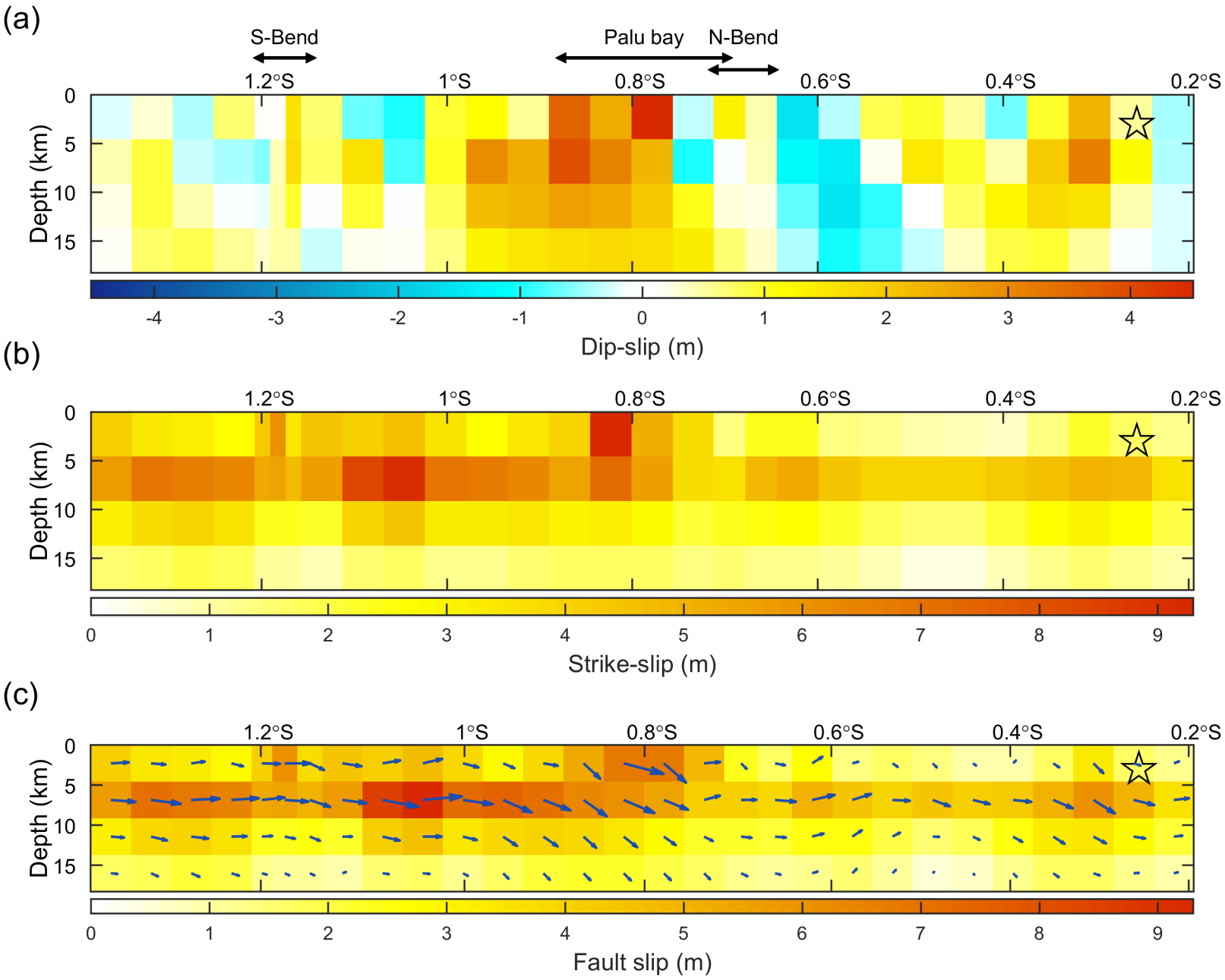
(a)
S-Bend
Palu bay
N-Bend
1.2°S
1°S
0.8°S
0.6°S
0.4°S
0.2°S
Depth (km)
0
5
10
15
-4
-3
-2
-1
0
1
2
3
4
Dip-slip (m)
(b)
1.2°S
1°S
0.8°S
0.6°S
0.4°S
0.2°S
Depth (km)
0
5
10
15
0
1
2
3
4
5
6
7
8
9
Strike-slip (m)
(c)
1.2°S
1°S
0.8°S
0.6°S
0.4°S
0.2°S
Depth (km)
0
5
10
15
0
1
2
3
4
5
6
7
8
9
Fault slip (m)

Figure 10.

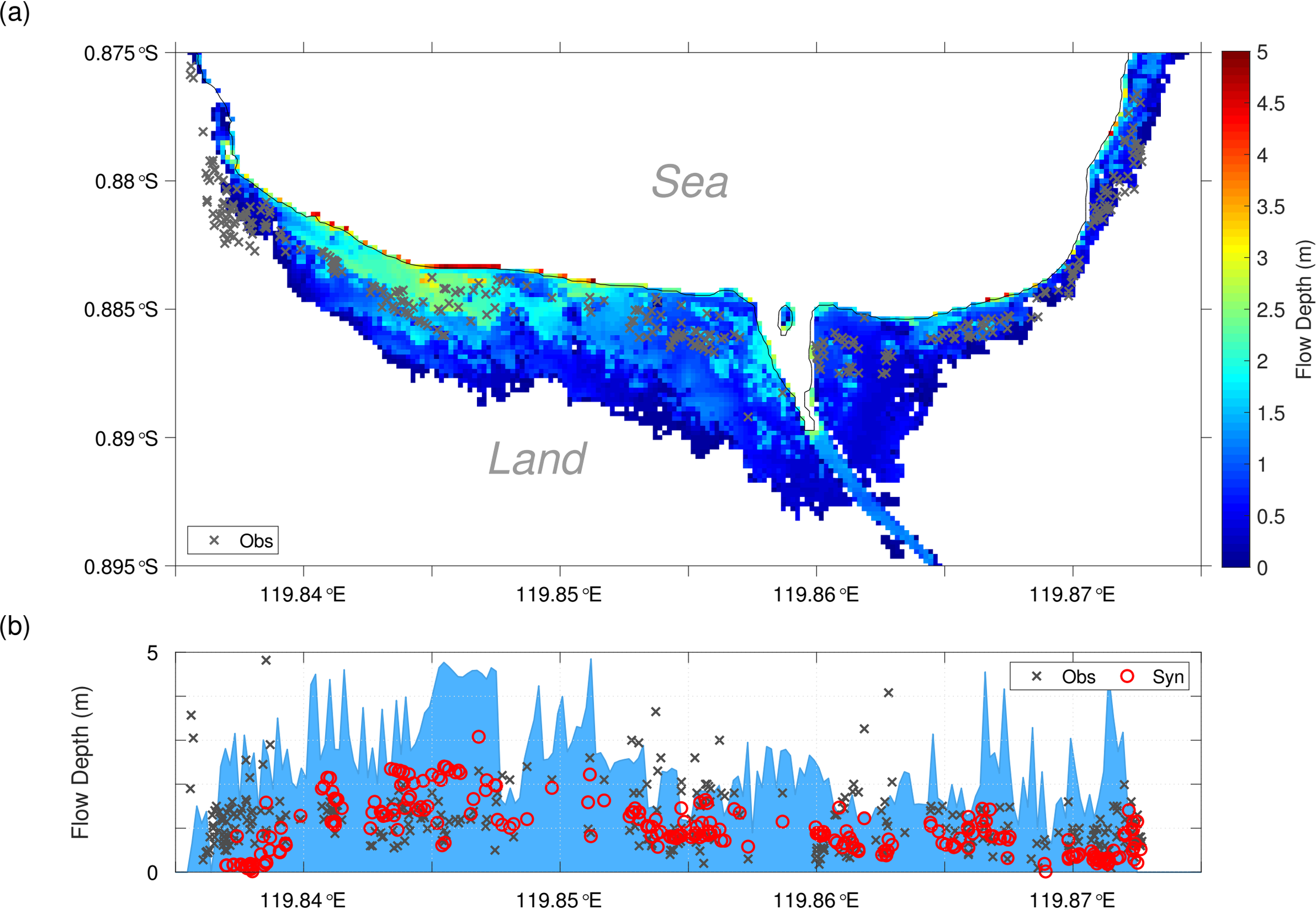
(a)
0.875 °S
0.88 °S
0.885 °S
0.89 °S
0.895 °S
119.84 °E
119.85 °E
119.86 °E
119.87 °E
Sea
Land
Obs
Flow Depth (m)
5
4.5
4
3.5
3
2.5
2
1.5
1
0.5
0
(b)
Flow Depth (m)
5
0
Obs
Syn
119.84 °E
119.85 °E
119.86 °E
119.87 °E

Figure 11.

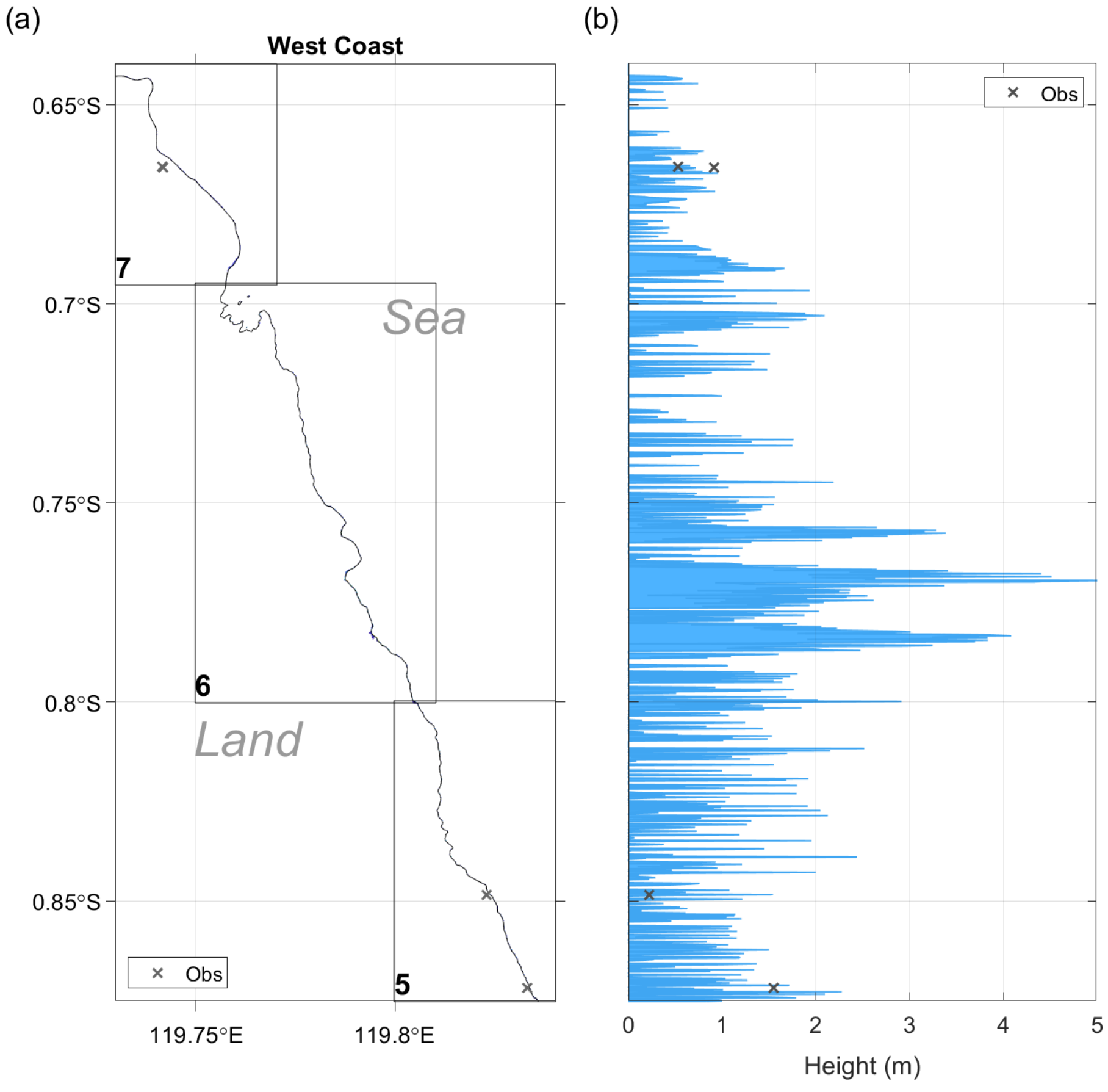
(a)
West Coast
0.65°S
0.7°S
0.75°S
0.8°S
0.85°S
7
6
5
Sea
Land
Obs
119.75°E
119.8°E
(b)
Obs
0
1
2
3
4
5
Height (m)

Figure 12.

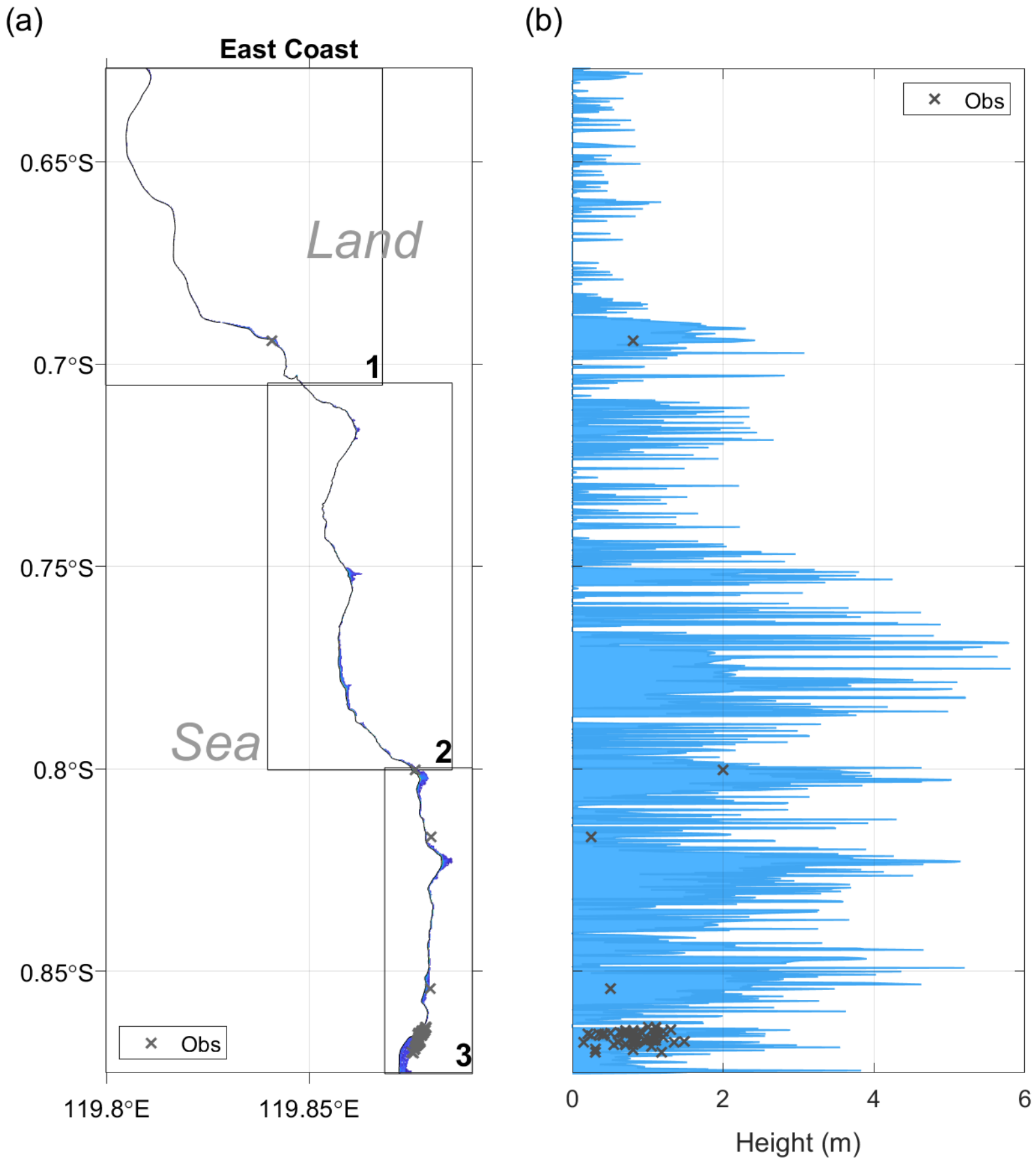
(a)
East Coast
0.65°S
0.7°S
0.75°S
0.8°S
0.85°S
Land
Sea
1
2
3
Obs
119.8°E
119.85°E
(b)
Obs
0
2
4
6
Height (m)